



**Perovskite Na-ion conductors developed from analogous
Li_{3x}La_{2/3-x}TiO₃ (LLTO): chemo-mechanical and defect
engineering**

Journal:	<i>Journal of Materials Chemistry A</i>
Manuscript ID	TA-ART-05-2021-004252.R2
Article Type:	Paper
Date Submitted by the Author:	20-Aug-2021
Complete List of Authors:	Lin, Yu-Ying; University of Illinois at Urbana-Champaign, Materials Science and Engineering Gustafson, William; University of Illinois at Urbana-Champaign, Mechanical Science and Engineering Murray, Shannon; University of Illinois at Urbana-Champaign, Materials Science and Engineering Shoemaker, Daniel; University of Illinois at Urbana-Champaign, Materials Science and Engineering Ertekin, Elif; University of Illinois, Department of Mechanical Science and Engineering Krogstad, Jessica; University of Illinois at Urbana-Champaign, Materials Science and Engineering Perry, Nicola; University of Illinois at Urbana-Champaign,

Perovskite Na-ion conductors developed from analogous $\text{Li}_{3x}\text{La}_{2/3-x}\text{TiO}_3$ (LLTO): chemo-mechanical and defect engineering

Yu-Ying Lin^{1,3}, William J. Gustafson^{2,3}, Shannon E. Murray^{1,3}, Daniel P. Shoemaker^{1,3}, Elif Ertekin^{2,3}, Jessica A. Krogstad^{1,3,*}, Nicola H. Perry^{1,3,*}

¹ Department of Materials Science and Engineering, University of Illinois at Urbana-Champaign, IL, USA

² Department of Mechanical Science and Engineering, University of Illinois at Urbana-Champaign, IL, USA

³ Materials Research Laboratory, University of Illinois at Urbana-Champaign, IL, USA

* Corresponding authors' emails: jakrogst@illinois.edu, nhperry@illinois.edu

Abstract

Na-ion conducting solid electrolytes can enable both the enhanced safety profile of all-solid-state-batteries and the transition to an earth-abundant charge-carrier for large-scale stationary storage. In this work, we developed new perovskite-structured Na-ion conductors from the analogous fast Li-ion conducting $\text{Li}_{3x}\text{La}_{2/3-x}\text{TiO}_3$ (LLTO), testing strategies of chemo-mechanical and defect engineering. $\text{Na}_x\text{La}_{2/3-1/3x}\text{ZrO}_3$ (NLZ) and $\text{Na}_x\text{La}_{1/3-1/3x}\text{Ba}_{0.5}\text{ZrO}_3$ (NLBZ) were prepared using a modified Pechini method with varying initial stoichiometries and sintering temperatures. With the substitution of larger framework cations Zr^{4+} and Ba^{2+} on B- and A-sites respectively, NLZ and NLBZ both had larger lattice parameters compared to LLTO, in order to accommodate and potentially enhance the transport of larger Na ions. Additionally, we sought to introduce Na vacancies through a) sub-stoichiometric Na:La ratios, b) Na loss during sintering, and c) donor doping with Nb. AC impedance spectroscopy and DC polarization experiments were performed on both $\text{Na}_{0.5}\text{La}_{0.5}\text{ZrO}_3$ and $\text{Na}_{0.25}\text{La}_{0.25}\text{Ba}_{0.5}\text{ZrO}_3$ in controlled gas environments (variable oxygen partial pressure, humidity) at elevated temperatures to quantify the contributions of various possible charge carriers (sodium ions, holes, electrons, oxygen ions, protons). Our results showed that the lattice-enlarged NLZ and NLBZ exhibited $\sim 19\times$ (conventional sintering) / $49\times$ (spark plasma sintering) and $\sim 7\times$ higher Na-ion conductivities, respectively, compared to unexpanded $\text{Na}_{0.42}\text{La}_{0.525}\text{TiO}_3$. Moreover, the Na-ion conductivity of $\text{Na}_{0.5}\text{La}_{0.5}\text{ZrO}_3$ is comparable with that of NaNbO_3 , despite having half the carrier concentration. Additionally, more than 96% of the total conductivity in dry conditions was contributed by sodium ions for both compositions, with negligible electronic conductivity and little oxygen ion conductivity. We also identified factors that limited Na-ion transport: NLZ and NLBZ were both challenging to densify using conventional sintering without the loss of Na because of its volatility. With spark plasma sintering, higher density can be achieved. In addition, the NLZ perovskite phase

1 appeared unable to accommodate significant Na deficiency, whereas NLBZ allowed some. Density
2 functional theory calculations supported a thermodynamic limitation to creation of Na-deficient NLZ in
3 favor of a pyrochlore-type phase. Humid environments generated different behavior: in
4 $\text{Na}_{0.25}\text{La}_{0.25}\text{Ba}_{0.5}\text{ZrO}_3$, incorporated protons raised total conductivity, whereas in $\text{Na}_{0.5}\text{La}_{0.5}\text{ZrO}_3$, they
5 lowered total conductivity. Ultimately, this systematic approach revealed both effective approaches and
6 limitations to achieving super-ionic Na-ion conductivity, which may eventually be overcome through
7 alternative processing routes.

9 1 Introduction

10 Lithium-ion batteries have developed rapidly in the past few decades to support their use in a variety
11 of applications, ranging from mobile devices to electric vehicles. However, the limited availability of
12 lithium is causing a significant shift in interest towards new types of rechargeable batteries, such as sodium-
13 based systems, because of their low cost and earth-abundance.¹ Furthermore, conventional liquid/polymer-
14 based electrolytes raise safety and manufacturing concerns, owing to their flammability and thermal
15 instability, limiting their application in mobile or large-scale systems such as electric vehicles and grid
16 storage.² As a result, solid electrolytes serve as a good replacement for current liquid and polymer-gel
17 electrolytes, owing to their high-temperature tolerance, longer lifetime, low toxicity, potential to enable
18 higher energy density electrodes, and simple cell design.³ For the reasons mentioned above, all-solid-state
19 sodium ion batteries are promising for next-generation energy storage systems, especially for large-scale
20 applications. Although significant developments have been made in solid electrolyte materials for sodium
21 ion transport such as the discovery of β'' -Alumina and NASICONs, practical issues such as high mechanical
22 stiffness, poor interface stability vs. high voltage electrodes, manufacturing challenges, and low room-
23 temperature conductivity still limit their applications in full cells.⁴⁻⁷ Alternative superionic conductors for
24 solid electrolyte materials in sodium batteries are clearly needed, and moreover, the strategies and design
25 principles for their development need to be established.

26 The double perovskite lithium-ion conductor system $\text{Li}_{3x}\text{La}_{2/3-x}\text{TiO}_3$ (LLTO) has been shown to
27 exhibit high ionic conductivity and a relatively wide electrochemical window.^{8,9} In addition, Ruddlesden-
28 Popper (RP) layered perovskites consisting of ABO_3 perovskite slabs with alkali ion layers are also potential
29 candidates for solid-state lithium-ion conductors.¹⁰ While sodium ion conduction has been investigated
30 between the interlayer planes of RP layered perovskites¹¹⁻¹³, sodium ion transport within ABO_3 perovskite
31 slabs in LLTO-type perovskites has not yet been widely studied.^{14,15} This omission is despite the fact that,

1 in general, ion transport within a perovskite is likely more 3-dimensional compared to that in RP-phase
2 interlayers, particularly if the perovskite is disordered.

3 In this study, we aimed to synthesize a new class of sodium ion conductors based on the LLTO-
4 type perovskite structure. Previous studies by Rivera et al.¹⁴ and Ruiz et al.¹⁵ suggested that Na⁺ conductivity
5 is low in an unsubstituted (i.e., La and Ti remain) or unexpanded LLTO structure. Because of the larger
6 ionic radius of sodium compared to lithium, we hypothesized that larger conduction channels are needed.
7 The lattice can be expanded for sodium ion conduction by the substitution of B- and A-site framework
8 cations with larger Zr⁴⁺ and Ba²⁺, respectively. With these substitutions, sodium lanthanum zirconate (NLZ)
9 and sodium lanthanum barium zirconate (NLBZ) were synthesized with similar but expanded structures to
10 LLTO perovskites for sodium ion conduction. Seeking to improve the level of sodium ion conductivity, we
11 varied the synthesis temperature, initial composition, and Nb dopant concentration, to manipulate the
12 relative density and defect chemistry, particularly the sodium sub-stoichiometry. The resulting
13 microstructures, phase compositions, and chemical compositions were analyzed in order to provide insights
14 into the structure-property relationships. Conductivities of NLZ and NLBZ were compared to investigate
15 the effect of different defect chemistries and lattice parameters. DC and AC electrical properties were also
16 systematically measured in various conditions (i.e., vs. oxygen partial pressure, humidity, temperature, and
17 with different electrodes) to identify charge carriers, determine transference numbers, and observe the
18 interactions between various possible carrier species (e.g., sodium ions, electrons, holes, oxygen ions,
19 protons). To better understand the results, density functional theory simulations were performed to evaluate
20 the stability of the new phases as a function of composition. We find that these materials exhibit
21 predominantly sodium ion conduction in dry, relatively oxidizing conditions; they are therefore new
22 sodium-ion-conducting solid electrolytes. The Na-ion conductivities of the enlarged NLZ and NLBZ
23 exceed that of the unexpanded Na_{0.42}La_{0.525}TiO₃ lattice by factors of ~19 (conventional sintering) / ~49
24 (spark plasma sintering) and ~7, respectively, and the conductivity of NLZ reaches a value similar to that
25 of NaNbO₃, despite the lower carrier concentration. We also conclude that ultimately, conductivity in bulk
26 samples is limited by kinetic challenges with densification and thermodynamic bounds on the sodium ion
27 deficiency that can be achieved in the perovskite phase. Based on these results, we suggest that non-
28 equilibrium synthesis routes to form metastable defect configurations within more dense structures may be
29 the best strategy forward for this class of Na-ion conductors, in future work.

30

2 Methods

2.1 Pellets fabrication

Sodium Lanthanum Zirconate (NLZ) (Formula: $\text{Na}_x\text{La}_{2/3-1/3x}\text{ZrO}_3$, abbreviated as NLZ-N_x), Sodium Lanthanum Barium Zirconate (NLBZ) (Formula: $\text{Na}_x\text{La}_{1/3-1/3x}\text{Ba}_{0.5}\text{ZrO}_3$, abbreviated as NLBZ-N_x), and Sodium Lanthanum Niobium Zirconate (Formula: $\text{Na}_x\text{La}_{2/3-1/3x}\text{Zr}_{1-y}\text{Nb}_y\text{O}_3$, abbreviated as NLBZ-N_x-N_{by}) nano-powders were synthesized by a modified Pechini method. Stoichiometric amounts of the starting reactants were dissolved in deionized water in a beaker, except that an extra 10% of $\text{Na}(\text{NO}_3)$ was added to compensate for Na loss during heat treatments in all compositions. Solutions were stirred for 30 minutes at 80 °C, followed by the addition of citric acid with stirring for 30 more minutes at 80 °C to allow chelation, followed by addition of ethylene glycol for polyesterification, with stirring at 80 °C until the solution became a gel. The molar ratios of Metal cations: Citric Acid: Ethylene glycol were 1: 3: 9 for all samples. After the polyesterification, the resin was dried at 240 °C for 10 hours (h). The dried gel was then crushed and calcined at 800 °C in air for 4 h. The NLZ and NLBZ pellets were fabricated by pressing the as-calcined powders uniaxially under 125 MPa with a hydraulic press (Carver, Model 4350). The compact green bodies were then sintered in a box furnace in air for various temperature and time combinations, as discussed in the results section. A tetragonal yttria stabilized zirconia (Formula: $(\text{ZrO}_2)_{0.97}(\text{Y}_2\text{O}_3)_{0.03}$, abbreviated as YSZ) pellet, used in transference number studies, was synthesized by pressing as-purchased YSZ powders (Sigma Aldrich, 99.99%) uniaxially under 125 MPa and sintering at 1200 °C in air for 6 h in a box furnace (YSZ-1200C 6hr). All sintering steps were carried out in sacrificial powders of the same compositions to minimize cation volatilization. Chemicals used include $\text{Na}(\text{NO}_3)$ (Sodium(I) Nitrate Anhydrous, Fisher Chemicals, 99%), $\text{La}(\text{NO}_3)_3 \cdot 6\text{H}_2\text{O}$ (Lanthanum(III) Nitrate Hydrate, Sigma-Aldrich, 99.99%), $\text{Ba}(\text{NO}_3)_2$ (Barium(II) Nitrate Anhydrous, Fisher Chemicals, 99.99%), $\text{ZrO}(\text{NO}_3)_2 \cdot x\text{H}_2\text{O}$ (Zirconium(IV) Oxynitrate hydrate, Sigma-Aldrich, 99 %), $(\text{NH}_4)\text{NbO}(\text{C}_2\text{O}_4)_2 \cdot x\text{H}_2\text{O}$ (Ammonium niobate(V) oxalate hydrate, Sigma-Aldrich, 99.99%), $\text{C}_6\text{H}_8\text{O}_7$ (Citric Acid Anhydrous, Fisher Chemicals, 99.5%), $(\text{CH}_2\text{OH})_2$ (Ethylene glycol, Fisher chemicals), and $(\text{ZrO}_2)_{0.97}(\text{Y}_2\text{O}_3)_{0.03}$ powders (Zirconium(IV) oxide-yttria stabilized, Sigma-Aldrich, 99.99%). Water contents of starting reagents were measured by separate mass-loss analysis.

2.2 Characterization

The densities of the samples were determined from measured masses and geometries of the pellets, and expressed in terms of their respective theoretical densities (measured density/theoretical density = %TD). The phases of NLZ and NLBZ pellets were examined by X-ray powder diffraction (XRD) (Bruker D8 Advance XRD, Cu $K\alpha$ -radiation, step size: 0.01°, time per step: 0.1 second, Panoramic Soller Slit) unless otherwise specified. High-resolution synchrotron powder diffraction data were collected using the rapid access program of beamline 11-BM at the Advanced Photon Source (APS), Argonne National

1 Laboratory with a wavelength of 0.458 Å on selected samples (step size: 0.001°, time per step: 1 second).
2 Rietveld refinements to all X-ray powder diffraction data were performed using TOPAS with Powder
3 Diffraction Files (PDF) from International Centre for Diffraction Data (ICDD) database¹⁶ for phase
4 quantification and lattice parameter refinement.

5 The microstructure and grain size of pellets were characterized by scanning electron microscopy
6 (JEOL 7000F Analytical SEM). For the electrical measurements, samples were coated on both faces with
7 electrodes, and Pt wires were attached as current collectors. Au electrodes deposited by sputtering are very
8 commonly used for cation conductors and were applied for all the measurements unless otherwise specified.
9 A systematic experimental comparison and discussion of the effect of electrode metal choice (Au, Ag, Pt)
10 is given in the Supporting Information (SI, Sec. 2). Two-point AC impedance spectroscopy measurements
11 (Ametek/Solartron ModulabXM ECS impedance analyzer with femtoammeter and potentiostat attachments)
12 were carried out from 300 °C to 600 °C in Ar/O₂ mixtures over a range of oxygen partial pressures under
13 dry or humid conditions. A water vapor pressure of 0.0121 atm was used in humid conditions by passing
14 gas mixtures through a bubbler containing deionized water at 10 °C. All ionic conductivity measurements
15 were carried out over a frequency range of 1 MHz to 100 mHz unless otherwise specified. The impedance
16 spectra were analyzed by equivalent circuit fitting with a (RQ) circuit (Boukamp notation) or observing the
17 low-frequency real axis intercept to determine the total resistance. A geometric correction according to the
18 dimensions of the pellets was done to calculate measured conductivity from the measured resistance. A
19 porosity correction was also performed based on Bruggeman symmetric medium theory, assuming pores to
20 be completely insulating.¹⁷⁻¹⁹ Impedance spectra were analyzed with a “Distribution of Relaxation Times”
21 (DRT) approach, using DRTtools software.²⁰ DC polarization experiments were performed using porous
22 sputtered Au electrodes and a constant applied voltage of 0.3 V, with monitoring of the current as a function
23 of time. Additional measurements and DRT analysis of the effect of different electrodes (Ag, Pt) can be
24 seen in Sec. 2 in SI.

25 The following abbreviations were used:

- 26 • NLZ-N_x powders: As calcined powders with cation ratio of Na: La: Zr = x: 2/3-1/3x: 1
27 (0 < x < 0.5).
- 28 • NLZ-N_x-(temperature time): NLZ-N_x powders pressed uniaxially under 125 MPa and
29 sintered at a certain temperature. For example, NLZ-N_{0.5}-(1200C 6hr) is sintered under
30 1200 °C for 6 hours.
- 31 • NLZ-N_x-N_y powders: As calcined powders with cation ratio of Na: La: Zr: Nb = x: 2/3-
32 1/3x: 1-y: y (0 < x < 0.5) (0 < y < 1).

- 1 • NLZ-N_x-N_y-(temperature time): NLZ-N_x-N_y powders pressed uniaxially under 125
2 MPa and sintered at a certain temperature. For example, NLZ-N_{0.5}-Nb_{0.05}-(1200C 6hr)
3 is sintered under 1200 °C for 6 hours.
- 4 • NLBZ-N_x powders: As calcined powders with cation ratio of Na: La: Ba: Zr = x: 1/3-1/3x:
5 0.5: 1 (0<x<0.25).
- 6 • NLBZ-N_x-(temperature time): NLBZ-N_x powders pressed uniaxially under 125 MPa and
7 sintered at a certain temperature. For example, NLBZ-N_{0.25}-(1200C 6hr) is sintered under
8 1200 °C for 6 hours.

9 2.3 Computation

10 Density functional theory^{21,22} calculations were performed using the Vienna *Ab Initio* Software
11 Package (VASP)^{23,24}. The Projector Augmented Wave (PAW) method was used to model the core electrons
12 in the crystal. The Perdew-Burke-Ernzerhof (PBE) generalized gradient approximation (GGA) to the
13 exchange-correlation functional was employed. The orbitals were expanded in a plane wave basis set with
14 an energy cutoff of 520 eV. For every compound that was simulated, geometry optimization was carried
15 out until the forces on each atom were reduced below 10⁻⁴ eV/Å. DFT-computed energies of both the
16 compounds under consideration as well as competing binaries, ternaries, and elemental phases were used
17 to create chemical potential and composition space phase diagrams.

18

19 3 Results

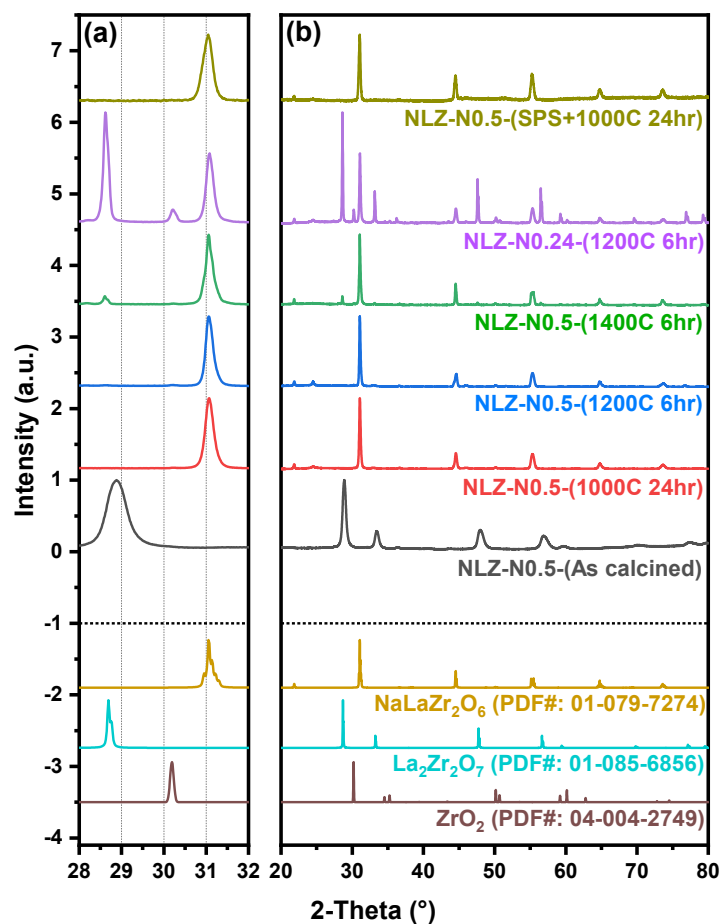
20 3.1 Structural Characterization

21 3.1.1 NLZ-N_x with different heat treatment and starting stoichiometry

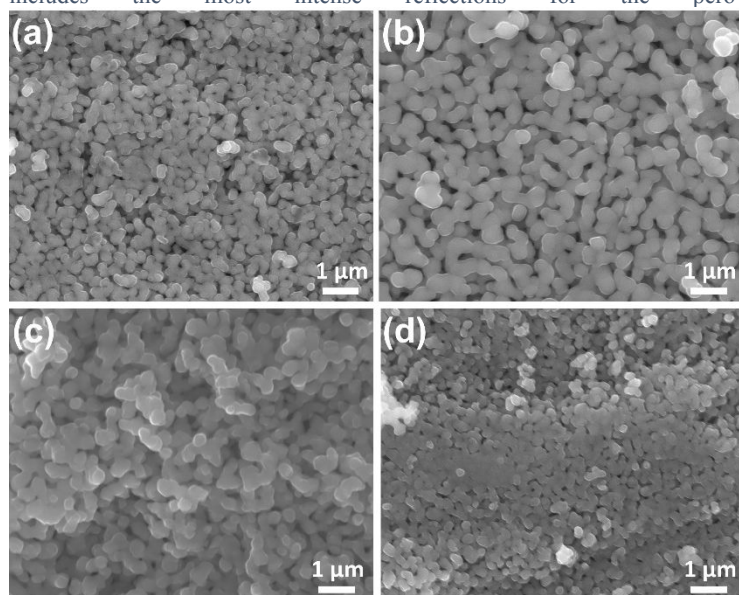
22 As described, all NLZ-N_x powders were synthesized by a modified Pechini method with a calcining
23 step of 800 °C for 4 h to keep the size of the particles small as well as preventing Na loss.²⁵ The XRD
24 patterns of NLZ-N_x powders and sintered pellets of different heat treatments and initial stoichiometry are
25 shown in Figure 1, and a summary of their phase fractions and densities can be seen in Table 1. It should
26 also be noted that a trace amount of an unidentified impurity phase was present in all sintered NLZ samples,
27 and the peak positions and broad width may be consistent with adventitious nanocrystalline carbonate-
28 hydroxide surface phase, given air exposure during XRD measurement. Due to the very minor peak
29 intensity, it is unlikely to have a significant effect on our analysis. The as-calcined powders were in a
30 distorted La₂Zr₂O₇-like pyrochlore phase before sintering. After sintering, a nominally pure Na_{0.5}La_{0.5}ZrO₃
31 perovskite phase was observed for sintering conditions of 1000 °C for 24 h and 1200 °C for 6 h, with similar

1 densities. The nominal stoichiometry given to the $\text{Na}_{0.5}\text{La}_{0.5}\text{ZrO}_3$ perovskite phase (and all other reported
2 perovskite phases) is presumed based on the targeted compositions and is used as a label to facilitate
3 consistent distinction between observed phases in XRD analysis. Chemical analysis by inductively coupled
4 plasma (ICP) also showed agreement with the nominal composition, within uncertainty (as determined by
5 replicate analysis). The average grain size increased from 252 nm to 375 nm when sintering temperature
6 was increased from 1000 °C to 1200 °C, as seen in Figure 2(a)(b). Sintering at 1400 °C for 6 h resulted in
7 higher density with a minor $\text{La}_2\text{Zr}_2\text{O}_7$ pyrochlore-like secondary phase. ICP also confirmed Na deficiency
8 after this higher temperature (1400 °C) sintering. To achieve higher density, spark plasma sintering (SPS)
9 was performed on NLZ-N0.5 powders at 700 °C and 500 MPa for 3 minutes, with a post-annealing step
10 using conventional sintering at 1000 °C for 24 h (abbreviated as NLZ-N0.5-(SPS+1000C 24hr)). XRD
11 showed a nominally pure $\text{Na}_{0.5}\text{La}_{0.5}\text{ZrO}_3$ perovskite phase, and a higher density of 73 ± 5 %. However, the
12 SPS treated sample was fragile and cracked into several small pieces, inevitably leading to some degree of
13 uncertainty in the geometry evaluation process. As a result, an error bar was included to indicate the level
14 of uncertainty for the density measurements. The microstructure of NLZ-N0.5-(SPS+1000C 24hr) also
15 appeared to be denser, with comparable grain size to NLZ-N0.5-(1000C 24hr), as seen in Figure 2(d).

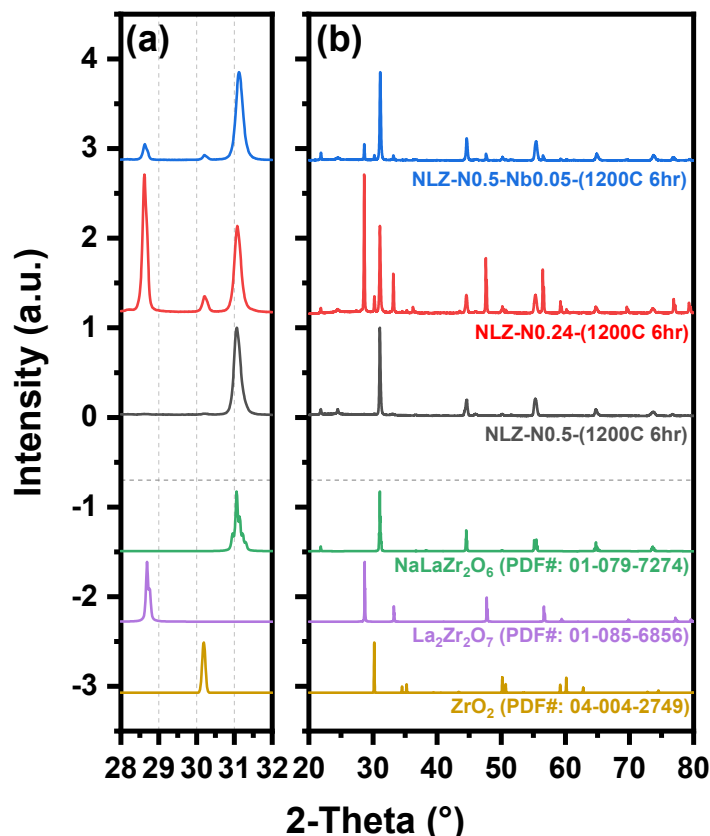
16 Intentionally Na-deficient NLZ-N0.24 powders were also synthesized using the same procedure
17 with different starting stoichiometry. After sintering under 1200 °C for 6 h, large amounts of $\text{La}_2\text{Zr}_2\text{O}_7$
18 pyrochlore-like phase and t- ZrO_2 -like phase were formed. For all these samples with different sintering
19 conditions and different starting stoichiometries, different amounts of impurity phases were formed;
20 however, the peak position of the $\text{Na}_{0.5}\text{La}_{0.5}\text{ZrO}_3$ perovskite phase remained unchanged. NLZ-N0.5 doped
21 with 5% of Nb was also prepared following the same synthesis procedure, with a stoichiometry of Na: La:
22 Zr: Nb= 0.5: 0.5: 0.95: 0.05 (NLZ-N0.5-Nb0.05). After sintering under 1200 °C for 6 h, 11.9 wt. % of
23 $\text{La}_2\text{Zr}_2\text{O}_7$ pyrochlore-like phase was formed. The peak positions of the Nb-doped perovskite phase were
24 also shifted to higher angles relative to the NLZ peaks as seen in Figure 3. Phase fractions and densities of
25 NLZ-Nx and NLZ-Nx-Nby are summarized in Table 1 according to different heat treatment and starting
26 stoichiometries.



1
 2 Figure 1: Experimental X-ray diffraction profiles for NLZ-N_x with different heat treatments and initial stoichiometries, and
 3 calculated XRD profiles from ICDD¹⁶ for the observed phases. The higher resolution data in the range of 2-Theta = 28°-32°
 4 includes the most intense reflections for the perovskite, pyrochlore and zirconia phases.



5
 6 Figure 2: SEM images of (a) NLZ-N0.5-(1000C 24hr), (b) NLZ-N0.5-(1200C 6hr), (c) NLBZ-N0.25-(1200C 6hr) and (d) NLZ-
 7 N0.5-(SPS+1000C 24hr).



1
2 *Figure 3: Experimental X-ray diffraction profiles for NLZ with different levels of doping, and calculated XRD profiles from ICDD¹⁶*
3 *for the observed phases. The higher resolution data in the range of 2-Theta = 28°-32° includes the most intense reflections for the*
4 *perovskite, pyrochlore and zirconia phases.*

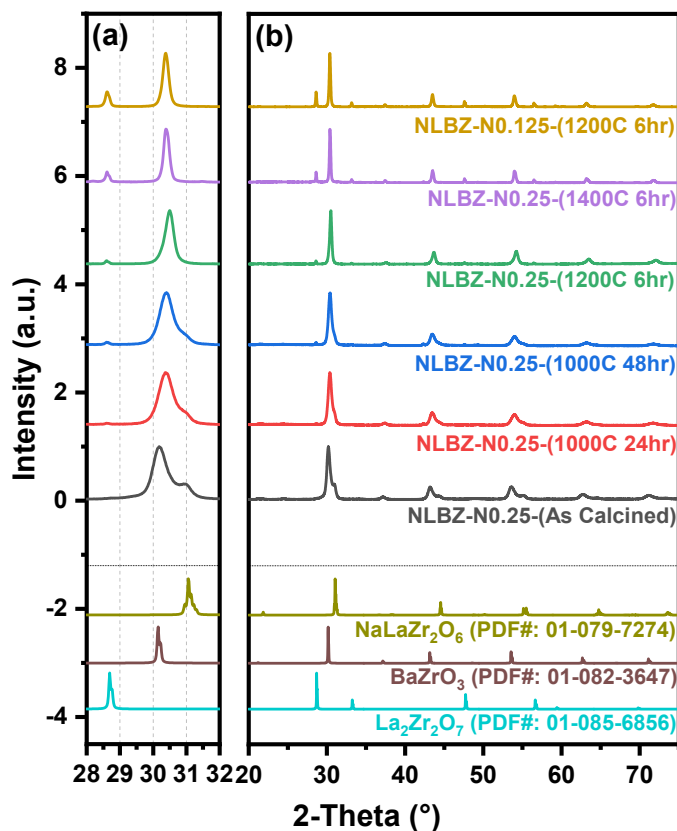
	Perovskite (wt. %)	Pyrochlore (wt. %)	t-ZrO ₂ (wt. %)	Density (% TD)	R _{wp} (%)
NLZ-N0.5-(1000C 24hr)	100	0.0	0.0	46.4	7.83
NLZ-N0.5-(1200C 6hr)	100	0.0	0.0	47.1	13.40
NLZ-N0.5-(1400C 6hr)	94.6	5.4	0.0	60.5	9.93
NLZ-N0.5-(SPS+1000C 24hr)	100	0.0	0.0	73 ± 5	7.96
NLZ-N0.24-(1200C 6hr)	46.1	45.9	8.0	-	11.20
NLZ-N0.5-Nb0.05-(1200C 6hr)	88.1	11.9	0.0	-	11.97

5 *Table 1: Phase fractions and densities of NLZ-N_x and NLZ-N_x-N_y with different heat treatments and initial stoichiometries. R_{wp}*
6 *values from Rietveld refinements are also listed here. (Tetragonal fluorite ZrO₂-like phase is abbreviated as t-ZrO₂. An unidentified*
7 *trace impurity phase was also detected in NLZ samples in XRD, but not included in refinement or listed in the table; see text.)*

8 3.1.2 NLBZ-N_x with different heat treatment and starting stoichiometry

9 NLBZ-N_x powders were synthesized using the same procedure as NLZ-N_x. The XRD data for the
10 NLBZ-N_x powders and sintered pellets after different heat treatment, as well as different starting Na
11 stoichiometries, are shown in Figure 4. The densities and phase fractions are further summarized in Table
12 2.

1 For the as-calcined NLBZ-N0.25 powders, XRD revealed a mixture of two perovskite phases,
2 which could be fitted to structures closely resembling BaZrO_3 and $\text{Na}_{0.5}\text{La}_{0.5}\text{ZrO}_3$. After sintering at 1000
3 °C for 24 h, the peaks of BaZrO_3 phase shifted to higher angles (lattice contracted), whereas the peaks of
4 $\text{Na}_{0.5}\text{La}_{0.5}\text{ZrO}_3$ shifted towards lower angles (lattice expanded), but both perovskite phases were retained.
5 Further heat treatment of 1000 °C for 48 h resulted in very little changes in the peak positions either
6 perovskite phase, while a slight increase in the amount of the $\text{La}_2\text{Zr}_2\text{O}_7$ -like pyrochlore phase was observed.
7 Sintering at 1200 °C for 6 h gave rise to a single perovskite phase with the nominal composition
8 $\text{Na}_{0.25}\text{La}_{0.25}\text{Ba}_{0.5}\text{ZrO}_3$ and density similar to NLZ-N0.5-(1200C 6hr). Minor formation of the $\text{La}_2\text{Zr}_2\text{O}_7$
9 pyrochlore-like phase was observed. The average grain size was measured to be 383 nm, as seen in Figure
10 2(c). Sintering at 1400 °C for 6 h resulted in a shift in the NLBZ perovskite peaks to lower angles and an
11 increase of $\text{La}_2\text{Zr}_2\text{O}_7$ pyrochlore-like phase fraction. The density also increased, consistent with NLZ-N0.5-
12 (1400C 6hr). As was the case for the NLZ compositions, samples of lower Na content in the starting
13 powders were also synthesized. XRD showed that NLBZ-N0.125-(1200C 6hr) was composed of a NLBZ
14 perovskite phase with the same peak positions as NLBZ-N0.25-(1400C 6hr) and 15.4 wt.% $\text{La}_2\text{Zr}_2\text{O}_7$
15 pyrochlore-like phase.



1
2 Figure 4: Experimental X-ray diffraction profiles for NLBZ-N_x with different heat treatments and initial stoichiometries, and
3 calculated XRD profiles from ICDD¹⁶ for the observed phases. The higher resolution data in the range of 2-Theta = 28°-32°
4 includes the most intense reflections for the perovskite, pyrochlore and zirconia phases.

	Perovskite (wt. %)	Pyrochlore (wt. %)	Density (% TD)	R _{wp} (%)
NLBZ-N0.25-(1200C 6hr)	98.0	2.0	44.5	9.23
NLBZ-N0.25-(1400C 6hr)	90.6	9.4	59.4	11.79
NLBZ-N0.125-(1200C 6hr)	84.6	15.4	45.4	10.89

5 Table 2: Phase fractions and densities of NLBZ-N_x with different heat treatments and initial stoichiometries. R_{wp} values from
6 Rietveld refinements are also listed here.

7 3.2 Electrical Measurements

8 Measured conductivity (σ_m) is calculated according to pellet geometry ($\sigma_m = R \cdot A / L$, where R is the
9 resistance, A is the electrode area, and L is the sample thickness). The low density of the sintered pellets
10 required that the measured conductivity data be corrected using the Bruggeman symmetric medium
11 theory¹⁷⁻¹⁹, where both high conductivity and low conductivity phases are assumed to be isotropic and non-
12 wetting to each other. In the case of porous samples, the high conductivity phase is the material itself,
13 whereas the low conductivity phase is the pore space, assumed to be completely insulating. As a result, the
14 porosity correction can be described by Eq. (1):

$$\sigma_m = \sigma_h \left[1 - \frac{3}{2}f \right] \quad (1)$$

σ_m is the measured conductivity, σ_h is the porosity corrected conductivity, representing the conductivity of the material matrix, and f is the volume fraction of the porosity.^{18,26} Impurity phases are also included and considered to be completely insulating.

Assuming a hopping mechanism, which most ionic conductors follow, the temperature-dependent conductivity can be described by the Arrhenius equation, and the activation energy can be calculated from the data by fitting with Eq. (2):

$$\sigma_h = \frac{\sigma_0}{T} \exp\left(\frac{-E_A}{k_B T}\right) \quad (2)$$

Here, σ_0 is the conductivity pre-factor, T is the temperature during measurements, E_A is the activation energy for ion hopping, and k_B is the Boltzmann constant.

3.2.1 Electrical properties of NLZ-N0.5-(1200C 6hr) and NLZ-N0.5-(SPS+1000C 24hr)

Electrical measurements for NLZ-N0.5-(1200C 6hr) were performed with porous Au electrodes unless otherwise specified. Figure 5(a) shows a typical Nyquist plot of NLZ-N0.5-(1200C 6hr) pellet with sputtered Au electrodes on both faces. The semicircle at high frequencies can be attributed to the sample response, whereas the feature at low frequencies is attributed to the electrode response. These attributions are made based on a) the relative permittivity of the high frequency feature obtained from the porosity-corrected capacitance (see SI Sec. 5) and b) the influence of electrode metal choice on the low frequency response (see SI Sec. 2). The high-frequency response attributed to the sample was first analyzed with a DRT approach, using DRTtools program²⁰; the results suggest only one relaxation time with Au electrodes (Fig. S5). Thus, the high-frequency arcs of the impedance spectra were analyzed with an (RQ) equivalent circuit in order to determine the total sample resistance, and the uncertainty in fitting was estimated to be within 5%-10%. The porosity-corrected relative permittivities (ϵ_r) of the sample response were between 294 and 252 in dry environments (300 °C-600 °C) for NLZ-N0.5-(1200C 6hr), which are comparable to those of similar perovskite compositions^{27,28}.

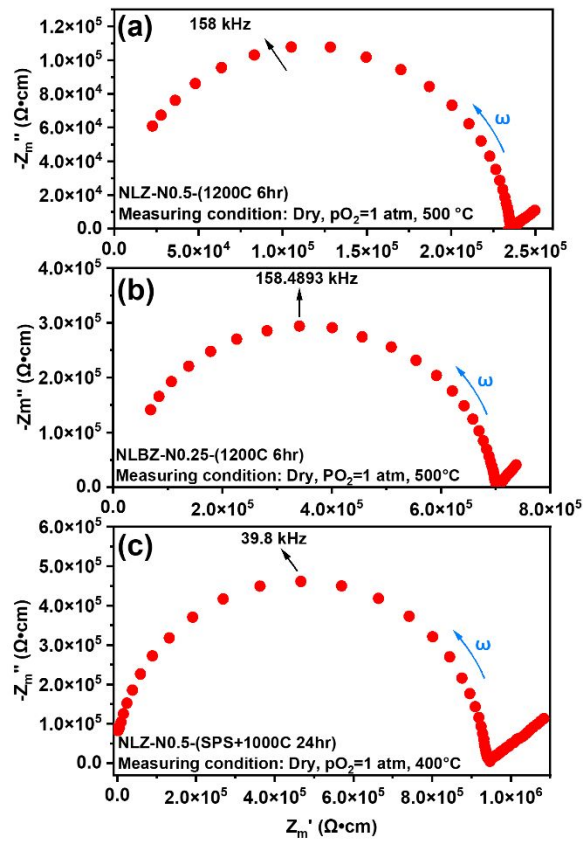
Measurements were performed under different pO_2 and different humidity at various temperatures to determine whether electronic species (holes, electrons) and/or protons contribute to total conductivities. The total conductivity in dry environments followed the Arrhenius equation very well, and the results were almost identical when measured under different pO_2 s ranging from 10^{-5} to 1 atm, as seen in Figure 6(a). At $pO_2=10^{-5}$ atm, the activation energy is calculated to be 0.80 eV; at $pO_2=1$ atm, the activation energy is calculated to be 0.81 eV; within error, these are the same. The porosity-corrected total conductivity of NLZ-

1 NLZ-N0.5-(1200C 6hr) is 4.25×10^{-7} S/cm at 300 °C. In humid environments, on the other hand, the conductivity
2 was very similar with the results from dry environments only in the high temperature range (400 °C-600
3 °C), whereas a decrease in conductivity was observed under humid conditions in the low temperature range
4 (300 °C-400 °C).

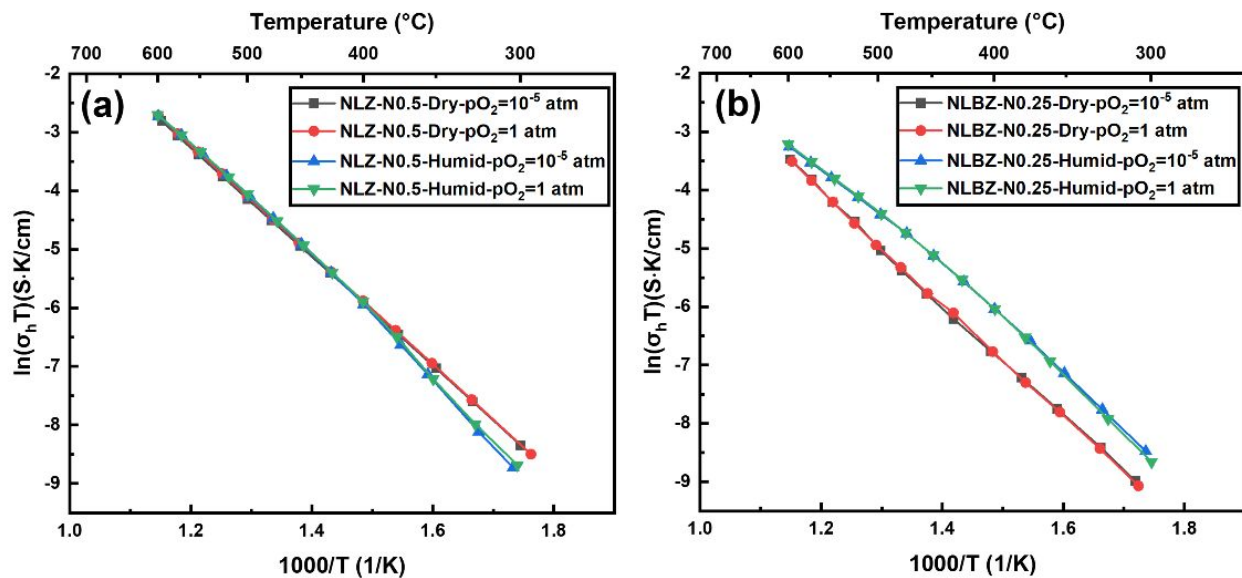
5 When total conductivity is measured by AC impedance spectroscopy, all mobile charge carriers
6 can contribute to the total conductivity. In dry environments measured with Au electrodes, four possible
7 species could have contributed to the total conductivity: sodium ions, oxygen ions, holes, and electrons.
8 Total conductivities for NLZ-N0.5-(1200C 6hr) were independent of pO_2 indicating that electronic defects
9 (electrons, holes) likely do not contribute significantly to the measured total conductivity, i.e., that
10 transference number (t_{elec}) were negligible. In order to determine the transference numbers of sodium ions
11 and oxygen ions, DC polarization experiments^{29,30} were first performed on YSZ-(1200C 6hr) using a
12 constant voltage of 0.3 V across the faces of the sample contacted with sputtered porous Au electrodes. The
13 current response was measured over time, as seen in Figure 7(c). With YSZ being a known oxygen-ion
14 conductor, the current was almost invariant over time, as the porous electrodes are not blocking to oxygen.
15 In order to quantify the transference number for oxygen conduction (t_o) of NLZ-N0.5-(1200C 6hr), the
16 same DC polarization experiments were performed. The current response was measured over time, as seen
17 in Figure 7(a). This was done at 600 °C in the dry condition under $pO_2 = 1$ atm. The current density
18 decreased and reached a plateau after 8×10^4 seconds, and $I_{final}/I_{initial}$ is calculated to be 0.0325. As sputtered
19 Au electrodes are only blocking to sodium ions, the sodium ion transference number (t_{Na}) is calculated to
20 be 0.9675. More detailed analysis of the transference numbers can be found in Sec.3 of the SI.

21 Additionally, AC impedance spectroscopy was also performed on NLZ-N0.5-(SPS+1000C 24hr).
22 Because of the fragile nature of the SPS sample (see Sec. 3.1.1), the handling of sample was kept to a
23 minimum, using Ag paste as electrodes, and measured in the range of 300 °C-400 °C in $pO_2=1$ atm. In the
24 case of NLZ-N0.5-(SPS+1000C 24hr) measured using Ag electrodes, only one arc was observed in the
25 impedance spectrum, as seen in Figure 5(c). DRT analysis also showed that there was only one process in
26 all the spectra (Figure S5(h)); more discussion concerning the feasibility of using Ag electrodes on this
27 denser sample can be found in Sec. 2 in the SI. The porosity-corrected conductivities of NLZ-N0.5-
28 (SPS+1000C 24hr) were higher than those of conventionally sintered NLZ-N0.5-(1200C 6hr), as seen in
29 Figure 8. The activation energy of NLZ-N0.5-(SPS+1000C 24hr) was calculated to be 0.81 eV, identical
30 with that of NLZ-N0.5-(1200C 6hr). Error bars were also included due to the uncertainty in
31 geometry/density evaluation because of the small sample size.

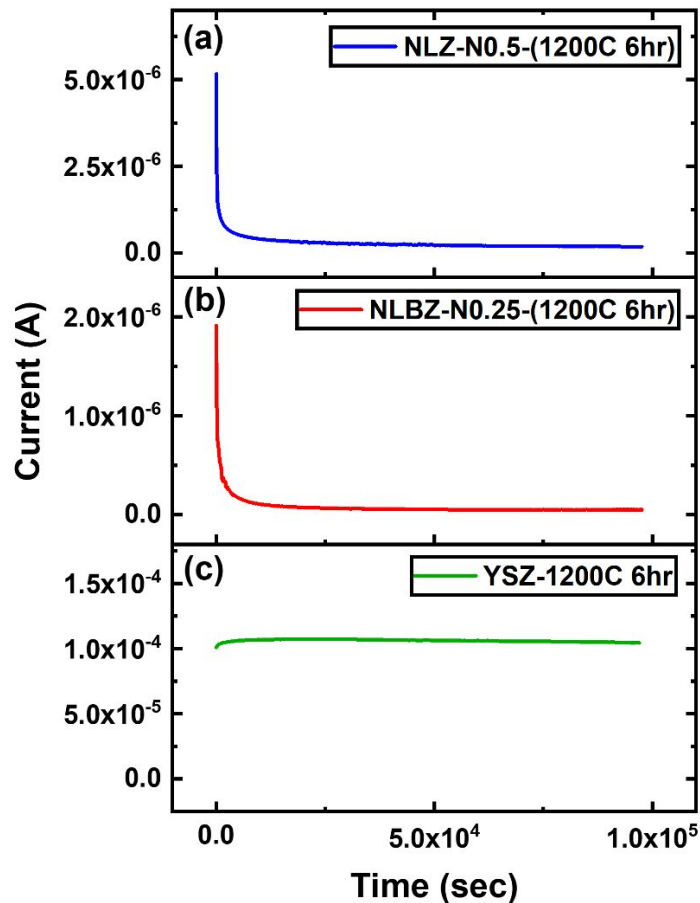
32



1
 2 Figure 5: Typical Nyquist plots of (a) NLZ-N0.5-(1200C 6hr), (b) NLBZ-N0.25-(1200C 6hr), (c) NLZ-N0.5-(SPS+1000C 24hr),
 3 measured in dry, $p_{\text{O}_2}=1$ atm gas environment at 500 °C. Z_m' and Z_m'' are respectively the real and imaginary part of the impedance
 4 that is geometry corrected and not porosity corrected.



5
 6 Figure 6: Arrhenius plots of porosity corrected total conductivity (σ_n) of (a) NLZ-N0.5-(1200C 6hr), (b) NLBZ-N0.25-(1200C 6hr)
 7 in different gas environments and humidity.



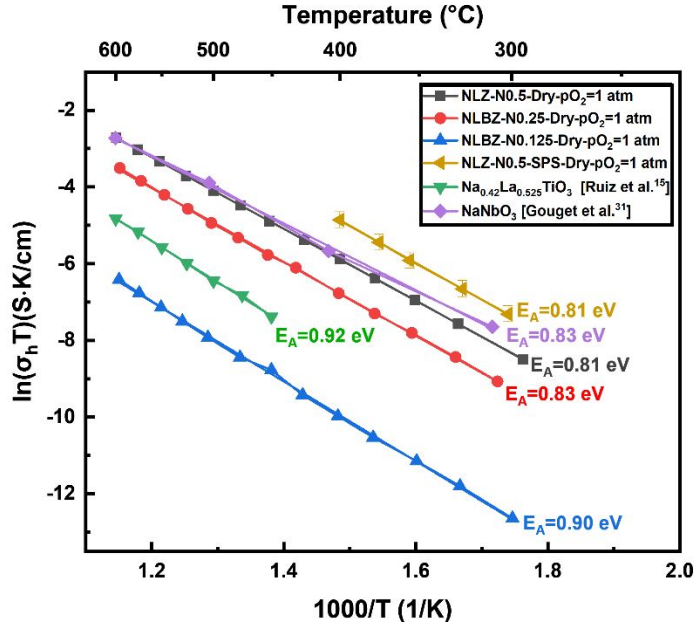
1
2 *Figure 7: Current response with respect to time under an applied voltage of 0.3V for (a)NLZ-N0.5-(1200C 6hr) (b) NLBZ-N0.25-*
3 *(1200C 6hr) (c)YSZ-(1200C 6hr) in dry, $pO_2= 1$ atm gas environment at 600 °C.*

4 3.2.2 Electrical properties of NLBZ-N0.25-(1200C 6hr)

5 Figure 5(b) shows a typical impedance spectrum of NLBZ-N0.25-(1200C 6hr) with sputtered Au
6 electrodes on both faces. Similar impedance spectra were observed for NLBZ-N0.25-(1200C 6hr) and the
7 earlier NLZ-N0.5-(1200C 6hr); therefore, the same procedures for fitting and measurements were used.
8 The relative permittivities (ϵ_r) of the sample response were between 1071 and 1411 in dry environments
9 (300 °C-600 °C) for NLBZ-N0.25-(1200C 6hr). The total conductivity in dry environments followed the
10 Arrhenius equation well and the results were very similar when measured under different pO_2 , from 10^{-5}
11 atm to 1 atm. Electrical measurements in dry environments under $pO_2=10^{-5}$ atm and $pO_2=1$ atm were almost
12 identical at all temperatures. At $pO_2=10^{-5}$ atm, the activation energy is calculated to be 0.83 eV; at $pO_2=1$
13 atm, the activation energy is calculated to be 0.83 eV, i.e., the same within error. The porosity-corrected
14 total conductivity of NLBZ-N0.25-(1200C 6hr) is 1.63×10^{-7} S/cm at 300 °C. In humid environments, the
15 conductivity was increased for both $pO_2 = 10^{-5}$ atm and $pO_2 = 1$ atm across the whole temperature range
16 (300 °C-600 °C), relative to the dry environments, as seen in Figure 6(b).

1 Similar to NLZ, the conductivities of NLBZ-N0.25-(1200C 6hr) are also not pO_2 dependent,
2 indicating negligible t_{elec} . The same DC polarization experiments were performed with the current response
3 measured as a function of time, as seen in Figure 7(b). At 600 °C in dry, $pO_2 = 1$ atm environment, the
4 current density reached a plateau after 8×10^4 seconds and $I_{final}/I_{initial}$ is calculated to be 0.0224. t_{Na} is
5 calculated to be 0.9776. Additional discussion on transference numbers can be seen in Sec. 3 of the SI.

6 Electrical measurements were also performed on NLBZ-N0.125-(1200C 6hr) with sputtered Au
7 electrodes in $pO_2 = 1$ atm and dry environments for comparison, to observe the effect of sodium deficiency.
8 Recall from Table 2 that this sample contained a larger amount of the minor pyrochlore phase and a slight
9 shift in perovskite phase XRD peaks relative to the NLBZ-N0.25-(1200C 6hr) sample. The pyrochlore
10 phase was assumed to be completely insulating in the conductivity magnitude correction process. The total
11 conductivity of the Na-deficient perovskite phase was significantly lower compared to both NLZ-N0.5-
12 (1200C 6hr) and NLBZ-N0.25-(1200C 6hr), as seen in Figure 8. Of note, both NLZ-N0.5-(1200C 6hr) and
13 NLBZ-N0.25-(1200C 6hr) exhibited significantly higher conductivities and lower activation energies
14 compared to non-expanded $Na_{0.42}La_{0.525}TiO_3$ (Ruiz et al.¹⁵), i.e., the case where Na simply substitutes for
15 Li in LLTO. At 300 °C, the conductivities were $\sim 19x$ and $\sim 7x$ higher for NLZ-N0.5-(1200C 6hr) and
16 NLBZ-N0.25-(1200C 6hr), respectively. The conductivity of NLZ-N0.5-(1200C 6hr) was also comparable
17 with that of $NaNbO_3$ (Gouget et al.³¹), which suffers from non-negligible oxygen ion conductivity.
18 Promisingly, although mechanically less robust, NLZ-N0.5-(SPS+1000C 24hr) was $\sim 49x$ more conductive
19 than $Na_{0.42}La_{0.525}TiO_3$ ¹⁵ at 300 °C. An in-depth discussion of these trends and magnitudes can be found in
20 Sec. 4.3.3.



1
2 Figure 8: Arrhenius plots of porosity corrected total conductivity (σ_h) of NLZ-N0.5-(1200C 6hr), NLBZ-N0.25-(1200C 6hr), NLBZ-
3 N0.125-(1200C 6hr), and NLZ-N0.5-(SPS+1000C 24hr) in dry $pO_2=1$ atm environment. Total conductivities of $Na_{0.42}La_{0.525}TiO_3$
4 (Ruiz et al.¹⁵) and $NaNbO_3$ (Gouget et al.³¹) are also shown here for comparison. Note that 12% of the conductivity of $NaNbO_3$
5 shown here is contributed by O^{2-} .³¹

6 4 Discussion and Supporting Simulations

7 4.1 Limits to Thermodynamic Stability and Defect Engineering of NLZ-Nx

8 One pillar of our strategy for producing Na-ion conducting perovskites was defect engineering, i.e.,
9 the intentional generation of Na vacancies (v_{Na}'). This route was pursued because it is known that in the
10 LLTO analogous structure, Li ions move by an A-site vacancy mechanism.^{8,9,32,33} To a first approximation,
11 an increased Na-vacancy concentration is therefore expected to raise the ionic conductivity pre-exponential
12 factor (σ_0) by increasing the availability of adjacent vacant sites for any given Na-ion to hop to. For isolated
13 ion hopping in a non-concerted mechanism, σ_h can be expressed as:

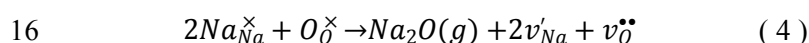
$$14 \quad \sigma_h = \frac{\gamma(Nc)Z(1-c)a^2(z_i e)^2 v_0}{k_B T} \exp\left(\frac{\Delta S_m}{k_B}\right) \exp\left(\frac{-\Delta H_m}{k_B T}\right) = \frac{\sigma_0}{T} \exp\left(\frac{-\Delta H_m}{k_B T}\right) \quad (3)$$

15 where γ is the geometric and correlation factor, N is the volumetric concentration of possible sites for the
16 charge carrier, c is the site fraction of the charge carrier, Z is the coordination number of the charge carrier
17 (number of nearest neighbor sites), a is the jump distance, $z_i e$ is the charge ($e=1.6 \times 10^{-19}$ C) of the charge
18 carrier i , v_0 is the jump attempt frequency, ΔS_m is the migration entropy, and ΔH_m is the migration enthalpy.³⁴
19 By introducing Na vacancies to a limited extent, the $c(1-c)$ term is increased, raising the σ_0 .

1 As noted previously, Na vacancies were pursued by three routes: 1) Na loss through long/hot
 2 sintering, 2) Na-deficient initial composition, and 3) Na vacancy generation through donor doping. The
 3 following sub-sections interpret the effectiveness of each of these approaches. We discuss the possible
 4 reasons for the phases and structures formed in the context of existing literature, the reasons for limits to
 5 Na vacancy formation in the perovskite phase with computational support, and the implications for transport.
 6 Synthesis of NLZ-N_x was carried out with two different starting stoichiometries: NLZ-N0.5 and NLZ-
 7 N0.24, along with different sintering conditions or Nb-doping for NLZ-N0.5. Prior to this work the
 8 Na_{0.5}La_{0.5}ZrO₃ phase had been synthesized for structural characterization and confirmed to be double
 9 perovskite³⁵⁻³⁷, but no electrical characterization was performed.

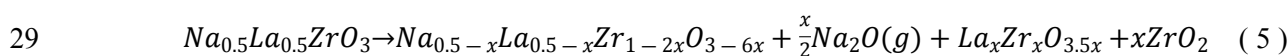
10 4.1.1 NLZ-N0.5: Controlling Na deficiency by sintering temperature and time

11 Longer/hotter sintering can result in overall Na deficient compositions, relative to the initial
 12 composition, given the reasonably high vapor pressure of Na₂O^{25,38}. To maintain electroneutrality, the v_{Na}'
 13 caused by loss of Na to the gas phase could be compensated ionically (e.g., by v_{O}'') or electronically (e.g.,
 14 by h^{\bullet}). As an example of the former case, a partial Schottky reaction might take place with loss of both Na
 15 and O at high temperatures:



17 If this reaction dominates, the simplified electroneutrality condition (ENC) would be $[v'_{Na}] \approx 2[v''_{O}]$.
 18 For the second option of electronic compensation, again if dominant, the simplified ENC would be $[v'_{Na}] \approx$
 19 $[h^{\bullet}]$. For both of these cases, one might expect additional ionic/electronic charge carriers to contribute to
 20 the overall measured conductivity; however, the selectively blocking electrode dc polarization
 21 measurements (section 3.2.1) demonstrated that conductivity was ~96% from Na ions. This result suggests
 22 that these reactions have not taken place to any significant degree, or are not dominant, or that charge-
 23 compensating defects are very deeply trapped. (In principle, Zr interstitial or anti-site defects could also
 24 charge-compensate for v_{Na}' formed by volatilization ($[v'_{Na}] \approx 4[Zr_i^{\bullet\bullet\bullet}]$ or $[v'_{Na}] \approx 3[Zr_{Na}^{\bullet\bullet}]$), but these
 25 defects are likely energetically unfavorable.)

26 When the desired perovskite phase is unstable at the composition of the overall Na deficiency,
 27 secondary phases can form. During high temperature Na loss, the excess La and Zr in the structure can
 28 leave the perovskite to form separate oxide phases, for example:



30 (In this example, the perovskite is assumed to be a line compound that maintains its initial stoichiometry,
 31 but in practice the composition will be pinned at the Na-deficient boundary of the thermodynamic stability.)

1 Other phases may also be observed in the context of kinetic limitations to perovskite phase formation during
2 initial synthesis stages.

3 In the NLZ-N0.5 starting stoichiometry, XRD showed that the as-calcined powders were in a
4 pyrochlore ($\text{La}_2\text{Zr}_2\text{O}_7$ -like) phase, but after pressing and sintering, the powders were transformed into a
5 $\text{Na}_{0.5}\text{La}_{0.5}\text{ZrO}_3$ perovskite phase. Since the NLZ-N0.5 powders were calcined at lower temperatures, and
6 the $\text{Na}_{0.5}\text{La}_{0.5}\text{ZrO}_3$ perovskite phase was formed after sintering, it is not likely that the pyrochlore phase for
7 the as-calcined powders was formed due to Na loss, when only minimal Na evaporation is expected at 800
8 °C.²⁵ Rather, this result indicates that the as-calcined NLZ-N0.5 powders were in a metastable pyrochlore
9 phase. A change in peak positions relative to pure $\text{La}_2\text{Zr}_2\text{O}_7$ was also observed, suggesting that the
10 pyrochlore phase was distorted vs. $\text{La}_2\text{Zr}_2\text{O}_7$, most likely due to a large amount of Na in the structure. After
11 sintering above 1000 °C, a pyrochlore–perovskite phase transformation occurred, resulting in a stable
12 $\text{Na}_{0.5}\text{La}_{0.5}\text{ZrO}_3$ perovskite phase. A further annealing step at 800 °C for 10 h did not result in any change in
13 the phase fraction, confirming that the $\text{Na}_{0.5}\text{La}_{0.5}\text{ZrO}_3$ perovskite phase is stable after sintering. Similar
14 behavior with a pyrochlore–perovskite phase transformation has been reported in $(\text{Pb},\text{La})(\text{Zr},\text{Sn},\text{Ti})\text{O}_3$
15 systems, where a metastable pyrochlore phase is first formed from an amorphous phase at lower
16 temperatures, and further heat treatment at higher temperature results in the formation of a perovskite
17 phase.³⁹

18 Our results at different sintering temperatures showed various amounts of the $\text{La}_2\text{Zr}_2\text{O}_7$ -like
19 pyrochlore impurity phase present. At 1000 °C for 24 h or 1200 °C for 6 h, the sintered pellet remained
20 phase pure with densities of 46.4% and 47.1%, respectively. The low densities can be attributed to the poor
21 sinterability of perovskite zirconate, as has been reported in some barium zirconate systems. A sintering
22 temperature of 1600 °C and the addition of dopants for solid-state reactive sintering are usually needed to
23 form dense samples of barium zirconate.^{40,41} Higher temperature sintering was thus performed at 1400 °C
24 for 6 h on pressed NLZ-N0.5 powders in order to increase the density of the pellet. The density was
25 increased to 60.8%; however, 5.4 wt. % of pyrochlore phase was formed due to Na loss under high sintering
26 temperature. The formation of a pyrochlore phase has also been reported in $\text{Li}_7\text{La}_3\text{Zr}_2\text{O}_{12}$ (LLZO) garnet-
27 type Li conductor due to a Li loss under heat treatments at higher temperatures.^{42,43} A longer heat treatment
28 for 96 h at a lower temperature of 1000 °C was also performed in an attempt to increase the density without
29 significant Na loss. However, there was little increase in grain size from an average of 252 nm to an average
30 of 280 nm between sintering for 24 h and 96 h at 1000 °C, no measurable change in density was observed,
31 and a slight amount of $\text{La}_2\text{Zr}_2\text{O}_7$ -like pyrochlore phase was formed. In these longer/hotter sintering
32 conditions with Na loss, the resulting pyrochlore phase appears more likely to be thermodynamically stable
33 unlike the peak-shifted metastable phase achieved following calcination of the precursor at lower

1 temperatures. In addition to conventional sintering, a higher density of $73 \pm 5 \%$ was achieved using SPS
2 followed by a post-annealing step, without $\text{La}_2\text{Zr}_2\text{O}_7$ -like pyrochlore phase formation. However, the SPS
3 treated sample suffered from residual stress, making the sample fragile and prone to crack. Fortunately, a
4 small piece of sample was still robust enough for electrical measurements. Furthermore, flash sintering was
5 attempted under an electric field of 20 V/mm and a ramp rate of 20 °C/min in a dog bone geometry, with
6 an identical setup demonstrated by Murray et al.⁴⁴, but the sample did not flash up to 950 °C. A higher
7 electric field of 40 V/mm was also attempted on a rectangular-shaped sample with Pt wires wrapped on the
8 ends of the sample; however, a bright light and popping noise occurred, and the wires on the positive
9 electrode had broken. These attempts resulted in inhomogeneous samples with large amounts of impurity
10 phases.

11 In LLTO, Li stoichiometry can be tuned in a relatively wide range through changing the Li:La and
12 thereby A:B-site ratios while maintaining the perovskite phase. Li deficiency has, to some degree, been
13 shown to yield a lower activation energy for ionic conduction. This effect can be attributed to an increase
14 of the lattice parameters due to the considerably larger lanthanum (1.032 Å) ion radius compared to that of
15 the lithium ion (0.76 Å)^{9,45}; here, Li deficiency is accommodated by excess La. In addition, the introduction
16 of Li vacancies (v_{Li}') also affects the conductivity by modifying the charge carrier concentration (if
17 considered to be vacancies) or available sites for hopping of carriers (if considered to be Li ions).^{9,45,46}
18 Despite the structural similarity to LLTO, the Na loss arising from higher temperatures or longer sintering
19 times for the NLZ-N0.5 starting stoichiometry instead resulted in the formation of the pyrochlore impurity
20 phase. The XRD peak positions of the NLZ perovskite phase were also examined for different sintering
21 conditions. Our results showed that there is no change in peak positions of the NLZ perovskite phase,
22 regardless of the amount of Na loss. It is possible that this invariability in peak position stemmed from very
23 limited Na stoichiometry change in the NLZ perovskite phase; in other words, the perovskite structure may
24 not be stable under Na deficient stoichiometry and thus allows very little v_{Na}' formation. It appears that
25 dense and phase pure $\text{Na}_{0.5}\text{La}_{0.5}\text{ZrO}_3$ has not been synthesized before, most likely due to these reasons. The
26 low density and likely low v_{Na}' concentration can explain some limitations to the ionic conductivity.

27 4.1.2 NLZ-N0.24: Generating Na deficiency by starting composition

28 As a second approach, NLZ-N0.24 with a Na-deficient starting stoichiometry was synthesized in
29 an effort to achieve a Na-deficient NLZ perovskite phase, thereby potentially increasing the conductivity
30 through the introduction of v_{Na}' . In this case, considering the NLZ-N0.5 as a reference state, the v_{Na}' are
31 charge-compensated by extrinsic addition of excess La on Na sites by design through maintenance of the x
32 : 2/3-1/3x ratio of Na : La in the synthesized composition. When this compensation mechanism is dominant,
33 the simplified ENC may be considered $[v'_{\text{Na}}] \approx 2[La\ddot{N}_a]$, with no generation of other ionic/electronic

1 carriers required. Again, the low oxide ion and electronic transference numbers measured (Section 3.2.1)
2 suggest that even other intrinsic / extrinsic defect reactions were also not significantly contributing these
3 carriers.

4 Sintering the NLZ-N0.24 powders at 1200 °C for 6 h resulted in a significant amount of $\text{La}_2\text{Zr}_2\text{O}_7$ -
5 like pyrochlore phase and t-ZrO₂-like phase, as shown in Table 1, which is to be expected on account of the
6 low Na content in the starting powders. Peak positions of the NLZ perovskite phase in NLZ-N0.24 were
7 examined carefully, and no deviations from the NLZ-N0.5 peak position were found. With low overall
8 sample Na content, the lattice parameters of the NLZ perovskite phase remained unchanged, corresponding
9 to our aforementioned results where hot sintering-induced overall Na deficiency resulted in pyrochlore
10 phase formation rather than a shift in the NLZ perovskite phase composition and peak position in NLZ-
11 N0.5. These results suggest a narrow (negligible) compositional width for the NLZ perovskite phase in
12 terms of the cation ratio.

13 4.1.3 NLZ-N0.5-Nb0.05: Targeting Na vacancies by donor doping

14 As a third approach, to further investigate the effect of Na stoichiometry on the NLZ perovskite
15 phase, 5% of Nb was doped onto the B-site in NLZ-N0.5 using the same procedure with the Pechini method;
16 we will abbreviate this composition as NLZ-N0.5-Nb0.05. A decrease in lattice parameters in the NLZ
17 perovskite phase was observed as expected, with Nb⁵⁺ (0.64 Å) having a smaller ionic radius compared to
18 Zr⁴⁺ (0.72 Å).⁴⁵ With the addition of Nb⁵⁺, Nb_{Zr}[•] is introduced into the NLZ perovskite phase, as Nb has
19 been shown to occupy the B-site in both lead barium zirconate (PBZ) and lead barium zirconate titanate
20 (PBZT) perovskite systems.^{47,48} In principle, with the introduction of the Nb_{Zr}[•] donor, the concentration of
21 positively charged defects such as v_O^{••} and h[•] may be suppressed, whereas the concentration of negatively
22 charged defects such as v_{Na}['] and e['] may be increased in the NLZ perovskite phase.⁴⁹ The goal here was
23 ionic compensation with $[v'_{Na}] \approx [Nb^*_{Zr}]$ resulting in negligible oxygen ion and electronic charge-carriers.
24 XRD showed that 5% of Nb doping in NLZ-N0.5 resulted in formation of 11.9 wt. % pyrochlore phase.
25 This result suggests that the donor doping induced Na deficiency in the sintered sample, but the NLZ
26 perovskite phase does not tolerate many v_{Na}['] within the structure. Therefore all three approaches to create
27 v_{Na}['] to improve the Na-ion conductivity resulted in secondary phase formation when Na-deficiency was
28 achieved, raising the issue of how the compositional width of the perovskite thermodynamic stability region
29 compares to that of the LLTO parent compound, which readily accommodates Li deficiency.

30 4.1.4 Thermodynamic stability and defect formation enthalpy of Na_{0.5}La_{0.5}ZrO₃

31 To analyze the thermodynamic stability of Na_{0.5}La_{0.5}ZrO₃, we used density functional theory to
32 obtain phase diagrams and assess the possibility of off-stoichiometry. Thermodynamic stability was

1 determined by obtaining the reaction decomposition energies for $\text{Na}_{0.5}\text{La}_{0.5}\text{ZrO}_3$ to other possible competing
 2 compounds in the chemical phase space. The possible competing compounds in the La-Na-Zr-O quaternary
 3 space were extracted from Materials Project⁵⁰, and only compounds within 40 meV per atom of the convex
 4 hull were included in our analysis. These competing compounds are NaO, Na_2O , $\text{La}_2\text{Zr}_2\text{O}_7$, NaLaO_2 , and
 5 ZrO_2 . For $\text{Na}_{0.5}\text{La}_{0.5}\text{ZrO}_3$, we simulated a double perovskite structure with an alternating, ordered
 6 arrangement of La and Na on the perovskite A-site as shown in Figure 9.

7 Different thermodynamic environments were accommodated by the set of chemical potentials μ_j
 8 for each element ($j = \text{La, Na, Zr, O}$). We referenced the chemical potential of each species to its
 9 corresponding chemical potential in the elemental phase $\mu_j = \mu_j^0 + \Delta\mu_j$. The standard formation enthalpy Δ
 10 H_f of $\text{Na}_{0.5}\text{La}_{0.5}\text{ZrO}_3$ represents the energy to form the compound from its constituent elemental phases^{51,52}
 11 and is given by,

$$12 \quad \Delta H_{\text{Na}_{0.5}\text{La}_{0.5}\text{ZrO}_3} = 0.5\Delta\mu_{\text{Na}} + 0.5\Delta\mu_{\text{La}} + \Delta\mu_{\text{Zr}} + 3\Delta\mu_{\text{O}} \quad (6)$$

13 For stability, it must not be favorable for the compound to decompose to either (i) a pure elemental phase
 14 or to (ii) a multi-species competing compound⁵¹. The first condition imposes the constraint that $\Delta\mu_j \leq 0$ for
 15 each element. The second condition imposes an additional constraint for each competing compound. For
 16 example, to avoid decomposition of $\text{Na}_{0.5}\text{La}_{0.5}\text{ZrO}_3$ to the competing phase NaO, the condition

$$17 \quad \Delta\mu_{\text{Na}} + \Delta\mu_{\text{O}} \leq \Delta H_{\text{NaO}} \quad (7)$$

18 must hold. If $\Delta H_{\text{NaO}} \leq \Delta H_{\text{Na}_{0.5}\text{La}_{0.5}\text{ZrO}_3}$, then NaO will likely form instead of $\text{Na}_{0.5}\text{La}_{0.5}\text{ZrO}_3$. Similar
 19 expressions must hold for all other stable competing compounds containing the elements La, Na, Zr, or O.

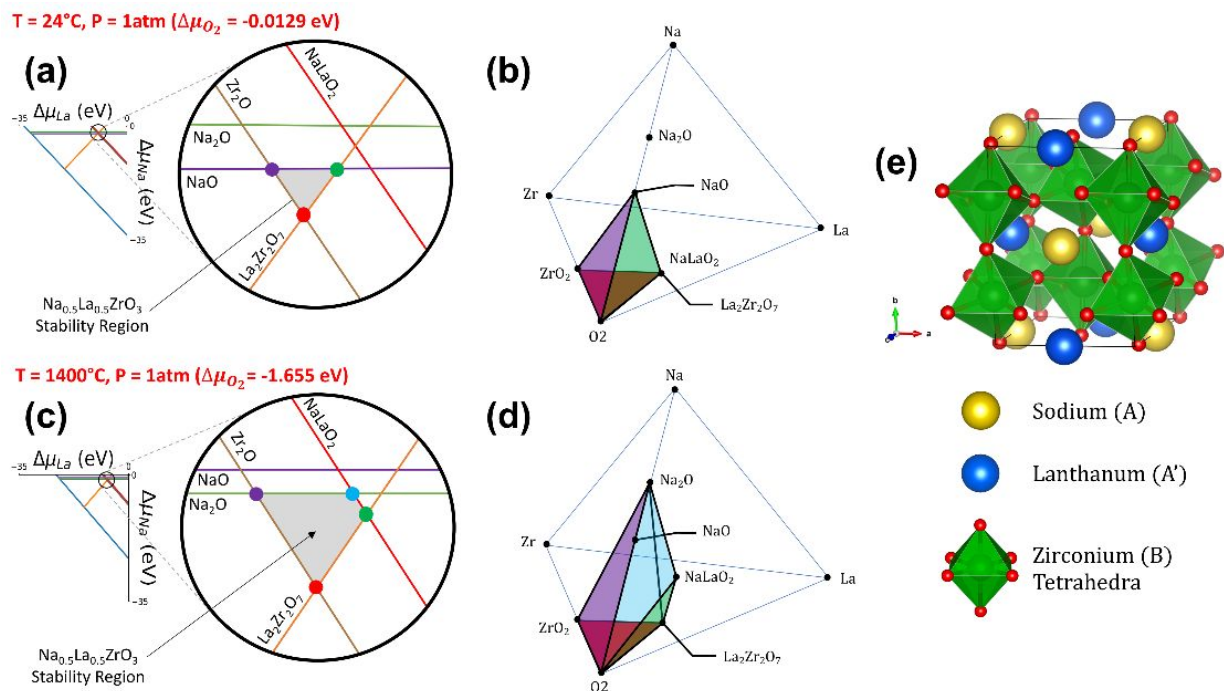
20 Figure 9 shows chemical potential and compositional phase diagrams for two values of the oxygen
 21 chemical potential that correspond to different temperatures: (i) $T=24^\circ\text{C}$, $P=1\text{ atm}$ and (ii) $T=1400^\circ\text{C}$, $P=1$
 22 atm. DFT calculations reveal a very small stability region for stoichiometric $\text{Na}_{0.5}\text{La}_{0.5}\text{ZrO}_3$ located near the
 23 top of the phase diagram, corresponding to a region of relatively high sodium and low lanthanum chemical
 24 potential. This suggests that $\text{Na}_{0.5}\text{La}_{0.5}\text{ZrO}_3$ will favor forming under sodium rich and lanthanum poor
 25 conditions and therefore will likely have difficulty forming a sodium deficient structure of $\text{Na}_{0.5}\text{La}_{0.5}\text{ZrO}_3$.
 26 As Figure 9(a)(c) show, under sodium poor conditions, the thermodynamic stability region is limited by the
 27 formation of pyrochlore $\text{La}_2\text{Zr}_2\text{O}_7$ and ZrO_2 . Thus, these phase diagram results corroborate the experimental
 28 findings that this double perovskite crystal structure may not accommodate sodium-deficient compositions,
 29 and that zirconia and the pyrochlore form in sodium-poor environments. The main difference between the
 30 two oxygen environments in Figure 9 is the upper phase boundary, which is limited by NaO at room
 31 temperature but by Na_2O at high temperature.

1 Figure 9(b)(d) show composition phase diagrams corresponding to the chemical potential phase
 2 diagrams in Figure 9(a)(c) respectively. Each shaded plane represents a base of an alkemade tetrahedron
 3 that represents a four-phase equilibrium between $\text{Na}_{0.5}\text{La}_{0.5}\text{ZrO}_3$, O_2 , and two other compounds. At $T=24$
 4 $^\circ\text{C}$, there are three possible four-phase equilibria: one with NaO and ZrO_2 , one with NaO and $\text{La}_2\text{Zr}_2\text{O}_7$,
 5 and one with $\text{La}_2\text{Zr}_2\text{O}_7$ and ZrO_2 . At $T=1400$ $^\circ\text{C}$, there are four possible four-phase equilibria: with Na_2O
 6 and ZrO_2 , with Na_2O and NaLaO_2 , with NaLaO_2 and $\text{La}_2\text{Zr}_2\text{O}_7$, and with $\text{La}_2\text{Zr}_2\text{O}_7$ and ZrO_2 .

7 Using the thermodynamic stability diagrams, we estimated the energy needed to introduce $2v'_{\text{Na}} +$
 8 $\text{La}_{\text{Na}}^{\bullet\bullet}$, two sodium vacancies adjacent to a $\text{La}_{\text{Na}}^{\bullet\bullet}$ antisite defect. This sodium deficient defect complex was
 9 considered because it retains charge neutrality based on ionic compensation. We introduced one $2v'_{\text{Na}} +$
 10 $\text{La}_{\text{Na}}^{\bullet\bullet}$ defect in a 40-atom supercell of $\text{Na}_{0.5}\text{La}_{0.5}\text{ZrO}_3$ and determined the defect formation energy according
 11 to

$$12 \quad \Delta E_f = (E_D - E_{\text{host}}) + 3\mu_{\text{Na}} - \mu_{\text{La}} \quad (8)$$

13 where E_D and E_{host} are respectively the computed energies of the defect-containing and perfect supercells.
 14 Using chemical potentials corresponding to the center of the thermodynamic stability region in Figure 9(a),
 15 the formation energy is found to be $\Delta E_f=2.63$ eV, extremely high for an ionic conductor. For comparison,
 16 a recent study in defect chemistry of the non-stoichiometric superionic conductor LGPS discovered the
 17 formation energy of a lithium vacancy to be on the order of 0.1 eV⁵³. According to Boltzmann statistics, a
 18 ΔE_f of 2.63 eV would correspond to a defect concentration of 7.1×10^{-24} per cm^3 at room temperature.



1
2 *Figure 9: (a) Calculated chemical potential phase diagram for $\text{Na}_{0.5}\text{La}_{0.5}\text{ZrO}_3$ at room temperature (24°C). Horizontal*
3 *and vertical axes correspond to chemical potentials of La and Na respectively. The chemical potential of O_2 is fixed*
4 *by the corresponding temperature and pressure. The purple, green, and red points in the circular schematic represent*
5 *four phase equilibria between the intersecting competing compound lines, $\text{Na}_{0.5}\text{La}_{0.5}\text{ZrO}_3$, and O_2 . (b) The*
6 *corresponding composition phase diagram at room temperature. The colors of the shaded planes correspond to the*
7 *points in the chemical potential phase diagram in part (a). (c) Chemical potential and (d) composition phase diagrams*
8 *at 1400°C . (e) Double perovskite crystal structure of $\text{Na}_{0.5}\text{La}_{0.5}\text{ZrO}_3$.*

9 In summary, with Na being a relatively volatile element at high temperatures, Na evaporation is a
10 limiting factor when it comes to selecting sintering conditions in NLZ. Perovskite zirconates are known to
11 have poor sinterability, making it very difficult to densify under lower sintering temperatures. In addition
12 to this kinetic limitation, we have also shown that the NLZ perovskite phase, unlike LLTO, does not
13 accommodate significant Na deficiency regardless of how that deficiency was introduced— by sintering
14 temperature, different starting Na stoichiometry and Na:La ratio, or Nb donor doping. Simulations also
15 demonstrated the high formation enthalpy of the Na vacancy when generated by a La anti-site defect. As a
16 result of these thermodynamic and kinetic factors, it is challenging to achieve simultaneously high density
17 and phase purity with NLZ. Moreover, the barriers to achieving density and Na deficiency may limit the
18 ionic conductivity of the perovskite.

19 4.2 Chemo-Mechanical and Defect Engineering: NLBZ-Nx

20 The second pillar of our strategy to create Na-ion conducting perovskites was to apply chemo-
21 mechanical engineering to chemically stretch the LLTO starting lattice to accommodate the larger Na-ion
22 that replaces Li. Increasing conductivity and decreasing activation energy have been reported in some Na-

1 ion conductors when their lattice parameters are expanded.^{54,55} We initially enlarged the lattice by replacing
2 the B-site Ti with larger Zr. To further enlarge to the conduction channels of NLZ systems, Ba was partially
3 introduced on the A sites, making the composition NLBZ-N_x (Na: La: Ba: Zr = x: 1/3-1/3x: 0.5: 1
4 (0 < x ≤ 0.25)), with Ba occupying half of the A sites. In addition to potentially expanding conduction
5 channels and lowering the activation energy, we also hypothesized that the inclusion of the larger Ba²⁺ (1.61
6 Å) could increase the stability of the perovskite structure, thereby allowing greater A-site deficiency.
7 Concomitant with this chemo-mechanical engineering strategy, we also pursued similar defect engineering
8 tactics as above to induce Na deficiency (heat treatment, varying Na:La ratio), with the goal of enhancing
9 v_{Na}' formation in the perovskite phase. In the following sub-sections, we interpret the phase composition
10 results for NLBZ-N_x, with particular emphasis on perovskite lattice dilation and A-site deficiency.

11 4.2.1 NLBZ-N0.25: Chemical Expansion

12 In the NLBZ-N0.25 starting stoichiometry, the composition is stoichiometric, and no initial A-site
13 deficiency is expected; however the impact of the 50% Ba A-site substitution on perovskite
14 symmetry/stability and lattice expansion is of interest. XRD revealed that a reaction occurred during
15 prolonged sintering. The as-calcined powders initially formed two perovskite phases with diffuse peaks.
16 These initial XRD patterns corresponded to those in the database for BaZrO₃ and Na_{0.5}La_{0.5}ZrO₃. After
17 sintering at 1000 °C for 24 h, the peak positions of the BaZrO₃ phase shifted to higher angles (the lattice
18 contracted), while those for the Na_{0.5}La_{0.5}ZrO₃ phase shifted to lower angles (the lattice expanded); i.e.,
19 they moved closer together, suggesting A-site cation interdiffusion between the two phases. Further heat
20 treatment at 1000 °C for 48 h resulted in little change. Two different perovskite phases were still discernable
21 and not fully reacted at this temperature, while the slight increase in La₂Zr₂O₇-like pyrochlore phase can be
22 attributed to prolonged sintering time and likely Na loss.

23 Sintering at 1200 °C for 6 h resulted in a full reaction between the two initial perovskite phases.
24 XRD analysis of this new phase, Na_{0.25}La_{0.25}Ba_{0.5}ZrO₃, revealed peak intensity ratios comparable to BaZrO₃,
25 with peak positions falling between those of the original BaZrO₃ and Na_{0.5}La_{0.5}ZrO₃ phases. However, there
26 was a peak shape difference. Analysis of our synchrotron data (Figure S1 and Figure S2) suggests that
27 Na_{0.25}La_{0.25}Ba_{0.5}ZrO₃ was in a cubic perovskite phase, whereas Na_{0.5}La_{0.5}ZrO₃ was orthorhombic with more
28 peak splitting.^{35,37} This result – both the lattice enlargement and increase in symmetry as Ba is substituted
29 on the A-site – is consistent with a simple tolerance factor analysis. The ability of a certain ABO₃
30 composition to form the perovskite phase stably has been described empirically through the Goldschmidt
31 tolerance factor, on the basis of the ionic radii. Values close to 1 indicate a more ideal cubic perovskite may
32 be formed, and the perovskite phase tends to form for values in the range 0.71-1.05; values near the edges
33 of this range might indicate structures with less ability to maintain the perovskite structure during

1 stoichiometric changes. NLBZ has a calculated tolerance factor of 0.9648, whereas for NLZ it is 0.9256.
2 The cell volume of $\text{Na}_{0.25}\text{La}_{0.25}\text{Ba}_{0.5}\text{ZrO}_3$ was increased to 71.23 \AA^3 , relative to the $\text{Na}_{0.5}\text{La}_{0.5}\text{ZrO}_3$ cell
3 volume of 67.32 \AA^3 . The relative density was measured to be 44.51% due to the poor sinterability of
4 perovskite zirconates at low temperatures. The barely discernable $\sim 2 \text{ wt. \%}$ $\text{La}_2\text{Zr}_2\text{O}_7$ -like pyrochlore phase
5 present could be due to an error in cation ratios during the modified Pechini synthesis process or slight Na
6 loss during sintering.

7 Heat treatment at a higher temperature of $1400 \text{ }^\circ\text{C}$ for 6 h achieved higher density, at the expense
8 of significant Na loss—consistent with the behavior of the NLZ system. The density was measured to be
9 63.3%, and the fraction of the $\text{La}_2\text{Zr}_2\text{O}_7$ -like pyrochlore phase increased to 9.36 wt. % as expected. The
10 peak positions of the NLBZ perovskite phase sintered at $1400 \text{ }^\circ\text{C}$ for 6 h were shifted to lower angles
11 compared to NLBZ-N0.25-(1200C 6hr), indicating an increase in lattice parameters from $a=4.145 \text{ \AA}$ to
12 $a=4.158 \text{ \AA}$ with the higher sintering temperature. The lattice expansion may be caused by Na vacancies on
13 the A-site in the NLBZ perovskite phase, with possible charge compensation from oxygen vacancies or
14 holes, for example, as discussed in section 4.1.1 above.^{56–58} Note that ionized oxygen vacancies or holes by
15 themselves are likely to contract the lattice^{57,59}, so any expansion in this case would be due to the v_{Na} . A-
16 site vacancies are usually larger compared to occupied A-sites.⁵⁸ (Based on the invariant conductivity vs.
17 $p\text{O}_2$ behavior, a high concentration of mobile holes is actually ruled out.) Hydration could also enlarge
18 lattice parameters via proton incorporation, but the measurements were performed under identical
19 conditions after sample storage in dry environments, suggesting that the samples sintered at different
20 temperatures did not have different proton concentrations as the primary reason underlying the strain. This
21 lattice expansion could therefore indicate that A-site deficient NLBZ is stable and possible to synthesize,
22 but the degree of A-site deficiency or A-site composition remains unknown. Na has the highest vapor
23 pressure of any of the cations (including Ba) for this composition, so it is the most likely candidate to cause
24 cation vacancies during heat treatments.

25 4.2.2 NLBZ-N0.125: Exceeding Limit of Na Deficiency

26 Following the same procedure on NLZ systems, non-stoichiometric NLBZ powders were
27 synthesized (NLBZ-N x powders, $x \neq 0.25$) with the goal of stabilizing more v_{Na} . First, NLBZ-N0.125
28 starting powders were pressed and sintered at $1200 \text{ }^\circ\text{C}$ for 6 h. XRD shows that the NLBZ-N0.125-(1200C
29 6hr) pellet is composed of two phases: primarily perovskite phase, with 15.4 wt. % of the pyrochlore-like
30 phase. The peak positions of the perovskite phase in the NLBZ-N0.125-(1200C 6hr) pellet line up well with
31 the peaks in NLBZ-0.25-(1400C 6hr) pellet. This agreement suggests that the NLBZ perovskite phase in
32 NLBZ-0.125 pellet was indeed A-site deficient, and the same limit of A-site deficiency was reached in the

1 perovskite phases within both NLBZ-N0.25-(1400C 6hr) and NLBZ-N0.125-(1200C 6hr) samples. Going
2 beyond this limit in the overall sample composition results in secondary phase formation.

3 In summary, the NLBZ perovskite phase may have more tolerance for Na deficiency compared to
4 NLZ. It is possible that the Ba²⁺ substitution in NLBZ indeed help stabilize the perovskite phase, allowing
5 some degree of v_{Na} as opposed to NLZ. Na-deficient NLBZ perovskite phase could be synthesized. It is,
6 however, still challenging to synthesize NLBZ without any La₂Zr₂O₇-like pyrochlore phase either via higher
7 sintering temperatures or lower initial Na stoichiometries. Similar to NLZ, NLBZ is also difficult to densify
8 using conventional sintering methods. The microstructure is porous, as can be seen in the SEM images
9 presented in Figure 2. Previous research has shown that the minor presence of an impurity phase does not
10 impact electrical conductivities significantly in lithium conductors and oxide ion conductors.^{60–62}
11 Impedance measurements can thus be performed on NLBZ-N0.25-(1200C 6hr) with minor pyrochlore
12 phase with necessary corrections, assuming the pyrochlore phase to be completely insulating.

13 4.3 Electrical Behavior: Impact of Stoichiometry, Lattice Size, and Humidity

14 4.3.1 Electrical properties of NLZ-N0.5-(1200C 6hr)

15 In dry environments, EIS and DC polarization measurements on NLZ-N0.5-(1200C 6hr) under
16 different pO₂ suggested that sodium ions were the primary carrier species, with negligible electronic
17 transference number (t_{elec}) and low oxygen-ion transference number (t_{O}). More discussion on transference
18 numbers can be seen in SI Sec. 3. The ionic conductivity was lower than that of LLTO; this difference can
19 at least partially be attributed to the low concentration of v_{Na} within the Na_{0.5}La_{0.5}ZrO₃ perovskite phase as
20 discussed in the previous sections. With a high concentration of Na sites occupied, sodium ion conduction
21 was likely impeded without available sites to hop into.

22 To determine how protons affect the total conductivity in gas atmospheres containing humidity,
23 electrical measurements for the same sample were performed in humid conditions also under different pO₂
24 at various temperatures. In the study of ionic conductors, it is important to separate the potential contribution
25 of protons; otherwise, the source of the total conductivity could be mis-identified. Certain oxygen-deficient
26 oxides have been shown to be able to incorporate protons in humid environments via oxygen vacancies^{63,64},
27 with water dissociating into oxygen vacancy and lattice oxygen sites being one possible mechanism as seen
28 in Eq. (9):



30 Additionally, some Li-ion conductors have been shown to undergo mobile cation exchange with
31 protons in acidic media or humid conditions, suggesting the possibility of proton diffusion/intercalation

1 along similar pathways to Li.⁶⁵⁻⁶⁷ With protons incorporated into the NLZ-N0.5-(1200C 6hr) in humid
2 environments, a decrease in conductivities was observed at low temperatures (300 °C-400 °C) in both
3 $pO_2=10^{-5}$ atm and $pO_2=1$ atm. This decrease might be attributed to the presence of protons disrupting Na
4 transport. Similar behavior has been seen in Li conductors, where water exposure and proton formation
5 have been shown to decrease conductivity in LLZO, as a result of protons being in the pathways of lithium
6 transport and disrupting the migration process.⁶⁸ Alternatively, the lower conductivity in humid conditions
7 could indicate sluggish proton transport along the Na pathways. When the measurement temperature was
8 raised to the higher temperature range (400 °C-600 °C), conductivities were identical in all conditions (e.g.
9 vs. pO_2 , humidity). We attribute this agreement to a dehydration reaction where protons were removed from
10 the lattice, causing the sample to be dehydrated even under humid conditions, with the effect of protons
11 diminished. From impedance measurements at different temperatures, it can be inferred that the dehydration
12 reaction occurred above 400 °C for NLZ-N0.5-(1200C 6hr), making transport properties similar for both
13 dry and humid conditions above 400 °C. Dehydration thermodynamics vary depending on the composition
14 of oxide proton conductors.⁶⁹⁻⁷¹

15 4.3.2 Electrical properties of NLBZ-N0.25-(1200C 6hr)

16 In dry environments, similar electrical behavior was observed in NLBZ-N0.25-(1200C 6hr)
17 compared to NLZ, with sodium-ions being the main carrier species; however, in humid conditions,
18 conductivities were independent of pO_2 and higher compared to dry conditions for any temperatures
19 between 300 °C and 600 °C, suggesting that the sample remains hydrated up to 600 °C under humid
20 conditions. Protons have been shown to act as additional carriers and give an increase in conductivity in
21 their hydrated state in certain compositions. For instance, $Ba_4In_2Zr_2O_{11}$ -based proton conductors showed
22 higher conductivity when hydrated.⁷² It can thus be inferred that NLBZ-N0.25-(1200C 6hr) was able to stay
23 hydrated in the range of 300 °C-600 °C, forming protons as additional conducting species, and possibly
24 transported via the Grotthuss mechanism. This opposite behavior compared to NLZ-N0.5-(1200C 6hr) may
25 be attributed to the presence of Ba^{2+} . Barium containing zirconates have been known to be able to
26 incorporate water and conduct protons more easily due to their low Bronsted basicity.^{73,74} It can also be
27 noted that the conductivity at higher temperature started to deviate from Arrhenius behavior above 400 °C,
28 which might be explained by some degree of dehydration. As the temperature increased, the magnitude of
29 increase in conductivity in humid environments vs. dry conditions decreased. This suggests that proton
30 concentration decreased with increasing temperature. Yttrium-doped barium zirconates have been shown
31 to exhibit similar proton conduction behavior, where dehydration and deviation of conductivity from
32 Arrhenius behavior was observed at higher temperatures.^{75,76}

1 To summarize, proton formation has opposite effects on conductivities of NLZ-N0.5-(1200C 6hr)
2 vs. NLBZ-N0.25-(1200C 6hr), with decreased conductivities at low temperatures (<400 °C) for the former,
3 and increased conductivities across the temperature range (300 °C-600 °C) for the latter. The difference of
4 conductivities vs. dry conditions in certain temperature ranges would suggest that the introduction of Ba
5 into the perovskite structure significantly modified proton formation and the dehydration process, with the
6 Ba-containing composition being able to incorporate protons over a larger temperature range. Our results
7 suggest that protons were blocking to Na transport and/or poorly mobile in the composition without Ba;
8 oppositely, protons were mobile and acted as an extra carrier species in the composition with Ba.

9 4.3.3 Comparison between NLZ-N0.5-(1200C 6hr), NLBZ-N0.25-(1200C 6hr), NLBZ-N0.125- 10 (1200C 6hr), and NLZ-N0.5-(SPS+1000C 24hr)

11 The conductivities of NLZ-N0.5-(1200C 6hr) and NLBZ-N0.25-(1200C 6hr) are shown in Figure
12 8; only dry conditions are compared here without the effect of protons. With both compositions having
13 larger cell volume (Sec. 4.2.1) compared to $\text{Na}_{0.42}\text{La}_{0.525}\text{TiO}_3$ (58.08 \AA^3)¹⁵, NLZ and NLBZ exhibited higher
14 σ_{h} and lower E_{A} compared to unexpanded $\text{Na}_{0.42}\text{La}_{0.525}\text{TiO}_3$ ¹⁵, as seen in Figure 8. This significant difference
15 suggests that the transport of Na ions can be effectively enhanced within ABO_3 perovskite slabs in LLTO-
16 type perovskites by enlarging of the lattice via a chemo-mechanical engineering approach. Moreover, the
17 conductivity of NLZ is also comparable with that of NaNbO_3 reported by Gouget et al.³¹, despite only
18 having half the carrier concentration compared to NaNbO_3 . NLZ also exhibits higher Na transference
19 numbers than NaNbO_3 . Even higher conductivity can be found in the densest sample fabricated using SPS,
20 NLZ-N0.5-(SPS+1000C 24hr). While the exact reason for this difference is not known, a few possible
21 contributors exist: a) SPS may modify the defect chemistry; b) there may be some inaccuracy in the porosity
22 correction applied to the more porous samples, given imperfectly spherical grains and pores; c) grain-to-
23 grain connections may be less constricted in the denser sample; and d) the grain sizes were different between
24 NLZ-N0.5-(SPS+1000C 24hr) NLZ-N0.5-(1200C 6hr). However, overall, the conductivities of NLZ and
25 NLBZ are still considerably lower compared to known Na super-ionic conductors like β'' -Alumina⁶ and
26 NASICONs⁷. More comparison of conductivity with other perovskite Na-ion conductors (including RP
27 phases) can be found in Sec. 4 in SI.

28 The total conductivity of NLBZ-N0.25-(1200C 6hr) is lower than that of NLZ-N0.5-(1200 C 6hr),
29 which can be explained by the lower concentration of Na. The conductivity pre-factor includes the carrier
30 concentration term, with Na ion concentration in NLBZ-N0.25-(1200C 6hr) being only half that of NLZ-
31 N0.5-(1200C 6hr). Experimentally, the conductivity pre-factor was decreased almost in half, resulting in a
32 decrease in total conductivity. Because of the larger lattice parameter in NLBZ-N0.25-(1200C 6hr), larger
33 conduction channels are also expected, which could result in a decrease in activation energy. However, our

1 results showed a very slight increase in activation energy, which may be within the margin of error.
2 Although rare, this counter-intuitive effect has also been seen in other cation conductors, where enlarged
3 conduction channels actually led to a decrease in ionic conductivity.⁷⁷ In addition, some researchers have
4 suggested that superionic conductors have optimal “percolation radii” for mobile cations, and the diffusion
5 channel should not be too small or too large.^{78,79} In the case of NLBZ-N0.25-(1200C 6hr), the conduction
6 channel may have been too large, starting to fall out of the range of the optimal percolation radius.
7 Nonetheless, other studies have observed no limit to the benefit of tensile strain for conductivity in cation
8 conductors.^{80–84} In the present work, an alternative factor that may account for the limited benefit from the
9 larger lattice relates to the local interactions: It is possible that the introduction of Ba resulted in a different
10 bonding environment for Na, where modified Coulombic interactions between Na and O cause Na-O bonds
11 to become stronger, countering the effect of the enlarged conduction channels.⁷⁷ In other words, chemo-
12 mechanical engineering should be applied carefully, considering the balance of macroscopic lattice strain
13 and local inhomogeneous atomic interaction effects.³⁴

14 Another interesting fact to be noted here is that the Nyquist plots for both NLZ-N0.5-(1200C 6hr)
15 and NLBZ-N0.25-(1200C 6hr), as seen in Figure 5, showed that there was only one arc. DRT analysis also
16 showed that there was only one process in all the spectra (Figure S5(d)) under different measurement
17 temperatures in dry conditions, where additional carriers such as protons and Ag are excluded. (The effect
18 of Ag and Pt electrodes can be seen in Sec. 2 in SI.) Although NLZ-N0.5-(1200C 6hr) and NLBZ-N0.25-
19 (1200C 6hr) were polycrystalline as can be seen in the SEM images, the impedance spectra did not show
20 different contributions from the grain core and the grain boundaries. Three hypotheses are proposed here
21 to explain this phenomenon: (1) the grain boundaries are not significantly blocking to cation transport in
22 the range of 300 °C – 600 °C, such that the response represents the bulk. For some cation conductors, grain
23 boundaries are blocking at low temperatures but cease to be significantly blocking at high temperatures due
24 to their higher activation energies, and the impedance spectra correspondingly can show a transition from
25 dual to single arc behavior, with a shrinking of the grain boundary arc, as temperature increases⁸⁵; or (2)
26 the relaxation time of the grain core and the grain boundaries were almost identical, making them
27 indistinguishable; or (3) the conduction primarily takes place in the vicinity of the surfaces/grain boundaries
28 in the porous microstructure, resulting in a fast path through the microstructure and only one process visible
29 in the impedance spectra. On the basis of the measured dielectric permittivities corresponding to this
30 impedance arc (see Sec. 3.2.1), we think that hypothesis (1) is reasonable.

31 Finally, the conductivity of NLBZ-N0.125-(1200C 6hr) was also measured with Au electrodes for
32 comparison. The pyrochlore phase was assumed to be completely insulating in the correction process. The
33 conductivity of the perovskite phase in NLBZ-N0.125-(1200C 6hr) is much lower compared to the other

1 samples, as seen in Figure 8. It is likely that the significant decrease in conductivity was a result of the
2 further decrease in Na-ion concentration.

3 5 Summary and Conclusion

4 In this work, $\text{Na}_{0.5}\text{La}_{0.5}\text{ZrO}_3$ and $\text{Na}_{0.25}\text{La}_{0.25}\text{Ba}_{0.5}\text{ZrO}_3$ were synthesized using a modified Pechini
5 method as a route to emulate the perovskite structure of the superionic lithium conductor LLTO. In order
6 to accommodate larger Na vs. Li ions, the lattices were expanded with the substitution of Zr^{4+} and Ba^{2+} on
7 the B- and A-sites of the original LLTO perovskite structure, respectively. In addition to this strain
8 engineering approach, we attempted to introduce v_{Na} systematically to improve the Na-ion conductivity,
9 by long/hot sintering, sub-stoichiometric Na:La and A:B site ratios, and donor doping. Although each of
10 these three methods charge-compensates for v_{Na} through different positively-charged defect species, our
11 XRD results indicated a common phenomenon: the NLZ structure could not accommodate significant A-
12 site deficiency, making it difficult to enhance the ionic conductivity without higher v_{Na} concentrations. On
13 the other hand, the Ba-containing NLBZ appeared to accommodate some degree of A-site deficiency,
14 though the minor formation of electrically insulating impurity phases could not be avoided when the Na
15 content further decreased beyond this limit. The poor sinterability typical of zirconates made it challenging
16 to densify NLZ and NLBZ without the loss of Na because of its volatility; as a result, impurity phases
17 tended to form when pursuing high densities using conventional methods. On the other hand, although the
18 sample was mechanically less robust, higher density and minimal Na loss could be achieved by an advanced
19 sintering technique like SPS.

20 In terms of electrical properties, both $\text{Na}_{0.5}\text{La}_{0.5}\text{ZrO}_3$ and $\text{Na}_{0.25}\text{La}_{0.25}\text{Ba}_{0.5}\text{ZrO}_3$ showed higher
21 conductivity and lower activation energy compared to unexpanded $\text{Na}_{0.42}\text{La}_{0.525}\text{TiO}_3$ ¹⁵, suggesting that the
22 lattice enlargement effectively boosted the mobility of Na ions. The conductivity of $\text{Na}_{0.5}\text{La}_{0.5}\text{ZrO}_3$ is also
23 comparable with NaNbO_3 ³¹, despite only having half the carrier concentration and a higher Na transference
24 number. Promisingly, the SPS-treated sample had even higher conductivity than those sintered
25 conventionally. $\text{Na}_{0.5}\text{La}_{0.5}\text{ZrO}_3$ exhibited higher ionic conductivity compared to $\text{Na}_{0.25}\text{La}_{0.25}\text{Ba}_{0.5}\text{ZrO}_3$,
26 which can be attributed to the lower Na-ion concentration of the latter composition. While the lattice
27 enlargement of the new $\text{Na}_{0.5}\text{La}_{0.5}\text{ZrO}_3$ relative to previously-reported $\text{Na}_{0.42}\text{La}_{0.525}\text{TiO}_3$ ¹⁵ helped to decrease
28 the conductivity activation energy, counter-intuitively, the expected further enlarged conduction channels
29 of $\text{Na}_{0.25}\text{La}_{0.25}\text{Ba}_{0.5}\text{ZrO}_3$ via partial substitution of Ba^{2+} on the A-site resulted in a similar E_A compared to
30 $\text{Na}_{0.5}\text{La}_{0.5}\text{ZrO}_3$. It is possible that this result stemmed from a deviation from optimal conduction channel
31 size and/or a difference in Na bonding environment. AC impedance spectroscopy measurements in dry
32 environments under different $p\text{O}_2$ s resulted in no change in total conductivity, suggesting negligible

1 electronic conductivity for both compositions, making them suitable for electrolyte applications. Moreover,
2 DC polarization experiments using reversible oxygen electrodes (porous gold) confirmed that oxygen ion
3 conductivities were also low for both compositions.

4 The effect of humidity was also investigated, with incorporated protons lowering the total ionic
5 conduction in $\text{Na}_{0.5}\text{La}_{0.5}\text{ZrO}_3$ in the low temperature range (300 °C-400 °C), and protons improving ionic
6 transport in $\text{Na}_{0.25}\text{La}_{0.25}\text{Ba}_{0.5}\text{ZrO}_3$ across the full temperature range (300 °C-600 °C). The introduction of
7 Ba^{2+} had a significant impact on the hydration/dehydration process; the proton transport properties and their
8 interaction with Na-ions were also altered appreciably.

9 Taken together, these results indicate that while strain and defect engineering are reasonable
10 strategies to turn a Li-ion conductor into new Na-ion conducting compositions, the intrinsic limitations of
11 a new composition – the kinetics of cation interdiffusion, cation vapor pressure, thermodynamic stability
12 bounds, and point defect formation enthalpies – may conspire to limit the electrical performance of the
13 resulting product, particularly using conventional sintering approaches close to thermodynamic equilibrium.
14 As a result, the conductivities of NLZ and NLBZ are likely too low in bulk ceramic, equilibrium form, for
15 room temperature batteries. However, given their stability at high temperatures in a wide range of $p\text{O}_2$, they
16 could still be of interest for higher temperature electrochemical cells used in large-scale stationary storage.
17 Furthermore, because the new compositions in the present study are almost pure Na-ion conductors with
18 low electronic conductivity in dry conditions, they may be worth synthesizing through alternative means.
19 Non-equilibrium routes, such as energetic thin film growth, may enhance relative density and quench-in
20 metastable defect concentrations in future work. We also emphasize the importance of verifying the nature
21 of the charge-carrying species in new solid electrolytes, given possible contributions from anions, electrons,
22 holes, and protons in addition to the desired mobile cation charge-carrier, and the importance of working
23 with suitably inert electrodes.

24

25 6 Acknowledgments

26 This material is primarily based upon work supported by the US Army CERL W9132T-19-2-0008
27 (to E.E. J.A.K. and N.H.P., also supporting Y.Y.L.). D.P.S. acknowledges research support by the
28 Army Research Office under Grant Number W911NF-17-1-0142. S.E.M. acknowledges support from the
29 National Science Foundation Graduate Research Fellowship Program under Grant No. DGE1144245. XRD,
30 SEM, and sputter coating were carried out in the Materials Research Laboratory Central Research Facilities,
31 University of Illinois. The authors also acknowledge the use of XRD instrumentation supported by NSF
32 through the University of Illinois Materials Research Science and Engineering Center DMR-1720633. Use

1 of the Advanced Photon Source at Argonne National Laboratory was supported by the U. S. Department of
2 Energy, Office of Science, Office of Basic Energy Sciences, under Contract No. DE-AC02-06CH11357.
3 The authors would like to thank Dr. Charles Smith and Nathan Madden (University of Illinois at Urbana-
4 Champaign) for their help with using spark plasma sintering as an alternative route to densify the pellet.

5

6 7 Supporting Information Description

- 7 • Synchrotron XRD data for NLZ-N0.5-(1200C 6hr) and NLBZ-N0.25-(1200C 6hr).
- 8 • Measurements with different electrodes.
- 9 • More discussion on transference numbers of different species.
- 10 • More comparison of the conductivities between this work and other perovskite Na-ion
11 conductors (including RP phases).
- 12 • Porosity corrected relative permittivity calculation.

13

14

15 8 Author Contributions

16 **Yu-Ying Lin**^{1,3}: Formal analysis, Investigation, Validation, Visualization, Writing - original draft, Writing
17 - review & editing, Project administration. **William J. Gustafson**^{2,3}: Formal analysis, Visualization,
18 Writing - original draft, Writing - review & editing. **Shannon E. Murray**^{1,3}: Investigation, Writing -
19 original draft. **Daniel P. Shoemaker**^{1,3}: Resources, Supervision, Funding acquisition. **Elif Ertekin**^{2,3}:
20 Resources, Methodology, Supervision, Writing - review & editing, Funding acquisition. **Jessica A.**
21 **Krogstad**^{1,3,*}: Conceptualization, Methodology, Resources, Supervision, Writing - review & editing,
22 Project administration, Funding acquisition. **Nicola H. Perry**^{1,3,*}: Conceptualization, Methodology,
23 Resources, Supervision, Writing - review & editing, Project administration, Funding acquisition.

24 **Declaration of interests:** The authors declare that they have no known competing financial interests or
25 personal relationships that could have appeared to influence the work reported in this paper.

26

27 9 References

- 28 1 A. M. Skundin, T. L. Kulova and A. B. Yaroslavtsev, *Russ. J. Electrochem.*, 2018, **54**, 113–152.
29 2 A. Ponrouch, D. Monti, A. Boschini, B. Steen, P. Johansson and M. R. Palacin, *J. Mater. Chem. A*,
30 2015, **3**, 22–42.

- 1 3 Z. Zhang, Y. Shao, B. Lotsch, Y.-S. S. Hu, H. Li, J. Janek, L. F. Nazar, C.-W. W. Nan, J. Maier, M.
2 Armand and L. Chen, *Energy Environ. Sci.*, 2018, **11**, 1945–1976.
- 3 4 K. B. Hueso, M. Armand and T. Rojo, *Energy Environ. Sci.*, 2013, **6**, 734.
- 4 5 Z. Zhang, Y. Shao, B. Lotsch, Y.-S. Hu, H. Li, J. Janek, L. F. Nazar, C.-W. Nan, J. Maier, M.
5 Armand and L. Chen, *Energy Environ. Sci.*, 2018, **11**, 1945–1976.
- 6 6 X. Lu, G. Xia, J. P. Lemmon and Z. Yang, *J. Power Sources*, 2010, **195**, 2431–2442.
- 7 7 N. Anantharamulu, K. Koteswara Rao, G. Rambabu, B. Vijaya Kumar, V. Radha and M. Vithal, *J.*
8 *Mater. Sci.*, 2011, **46**, 2821–2837.
- 9 8 Y. Sun, P. Guan, Y. Liu, H. Xu, S. Li and D. Chu, *Crit. Rev. Solid State Mater. Sci.*, 2019, **44**, 265–
10 282.
- 11 9 C. H. Chen and J. Du, *J. Am. Ceram. Soc.*, 2014, **98**, 534–542.
- 12 10 P. Ramakrishnan, H. Kwak, Y. H. Cho and J. H. Kim, *ChemElectroChem*, 2018, **5**, 1265–1271.
- 13 11 K. Toda, Y. Kameo, S. Kurita and M. Sato, *J. Alloys Compd.*, 1996, **234**, 19–25.
- 14 12 A. A. Petrov, N. A. Melnikova, A. V. Petrov, O. I. Silyukov, I. V. Murin and I. A. Zvereva, *Ceram.*
15 *Int.*, 2017, **43**, 10861–10865.
- 16 13 S.-H. Byeon, K. Park and M. Itoh, *J. Solid State Chem.*, 1996, **121**, 430–436.
- 17 14 A. Rivera, C. León, J. Santamaría, A. Várez, O. V'yunov, A. G. Belous, J. A. Alonso and J. Sanz,
18 *Chem. Mater.*, 2002, **14**, 5148–5152.
- 19 15 A. I. Ruiz, M. L. López, C. Pico and M. L. Veiga, *J. Solid State Chem.*, 2002, **163**, 472–478.
- 20 16 S. Gates-Rector and T. Blanton, *Powder Diffr.*, 2019, **34**, 352–360.
- 21 17 D. A. G. Bruggeman, *Ann. Phys.*, 1935, **416**, 636–664.
- 22 18 D. S. McLachlan, M. Blaszkiewicz and R. E. Newnham, *J. Am. Ceram. Soc.*, 1990, **73**, 2187–2203.
- 23 19 W. Pabst and E. Gregorová, *J. Eur. Ceram. Soc.*, 2014, **34**, 2757–2766.
- 24 20 T. H. Wan, M. Saccoccio, C. Chen and F. Ciucci, *Electrochim. Acta*, 2015, **184**, 483–499.
- 25 21 P. Hohenberg and W. Kohn, *Phys. Rev.*, 1964, **136**, B864–B871.
- 26 22 W. Kohn and L. J. Sham, *Phys. Rev.*, 1965, **140**, A1133–A1138.
- 27 23 G. Kresse and J. Furthmüller, *Phys. Rev. B*, 1996, **54**, 11169–11186.
- 28 24 G. Kresse and J. Furthmüller, *Comput. Mater. Sci.*, 1996, **6**, 15–50.
- 29 25 M. Li, T. Utigard and M. Barati, *Metall. Mater. Trans. B*, 2015, **46**, 74–82.
- 30 26 S. JO, *Solid State Ionics*, 2008, **178**, 1990–1997.
- 31 27 R. Gu, K. Yu, L. Wu, R. Ma, H. Sun, L. Jin, Y. Xu, Z. Xu and X. Wei, *Ceram. Int.*, 2019, **45**, 8243–
32 8247.
- 33 28 K. Yu, Y. Tian, R. Gu, L. Jin, R. Ma, H. Sun, Y. Xu, Z. Xu and X. Wei, *J. Eur. Ceram. Soc.*, 2018,
34 **38**, 4483–4487.

- 1 29 S. Lunghammer, D. Prutsch, S. Breuer, D. Rettenwander, I. Hanzu, Q. Ma, F. Tietz and H. M. R.
2 Wilkening, *Sci. Rep.*, 2018, **8**, 11970.
- 3 30 K. Kataoka, H. Nagata and J. Akimoto, *Sci. Rep.*, 2018, **8**, 9965.
- 4 31 G. Gouget, F. Mauvy, U.-C. Chung, S. Fourcade, M. Duttine, M.-D. Braida, T. Le Mercier and A.
5 Demourgues, *Adv. Funct. Mater.*, 2020, **30**, 1909254.
- 6 32 X. Gao, C. A. J. Fisher, T. Kimura, Y. H. Ikuhara, H. Moriwake, A. Kuwabara, H. Oki, T.
7 Tojigamori, R. Huang and Y. Ikuhara, *Chem. Mater.*, 2013, **25**, 1607–1614.
- 8 33 H. Moriwake, X. Gao, A. Kuwabara, C. A. J. Fisher, T. Kimura, Y. H. Ikuhara, K. Kohama, T.
9 Tojigamori and Y. Ikuhara, *J. Power Sources*, 2015, **276**, 203–207.
- 10 34 Y.-Y. Lin, A. X. Bin Yong, W. J. Gustafson, C. N. Reedy, E. Ertekin, J. A. Krogstad and N. H.
11 Perry, *Curr. Opin. Solid State Mater. Sci.*, 2020, **24**, 100875.
- 12 35 M. C. Knapp and P. M. Woodward, *J. Solid State Chem.*, 2006, **179**, 1076–1085.
- 13 36 M. C. Knapp, The Ohio State University, 2006.
- 14 37 S. García-Martín, E. Urones-Garrote, M. C. Knapp, G. King and P. M. Woodward, *MRS Proc.*, 2008,
15 **1148**, 1148-PP15-05.
- 16 38 R. H. Lamoreaux and D. L. Hildenbrand, *J. Phys. Chem. Ref. Data*, 1984, **13**, 151–173.
- 17 39 J. Lee and Y. Chiang, *J. Mater. Chem.*, 1999, **9**, 3107–3111.
- 18 40 J. Tong, D. Clark, M. Hoban and R. O’Hayre, *Solid State Ionics*, 2010, **181**, 496–503.
- 19 41 J. Tong, D. Clark, L. Bernau, A. Subramaniyan and R. O’Hayre, *Solid State Ionics*, 2010, **181**, 1486–
20 1498.
- 21 42 I. Kokal, M. Somer, P. H. L. Notten and H. T. Hintzen, *Solid State Ionics*, 2011, **185**, 42–46.
- 22 43 M. Kotobuki, K. Kanamura, Y. Sato and T. Yoshida, *J. Power Sources*, 2011, **196**, 7750–7754.
- 23 44 S. E. Murray, T. J. Jensen, S. S. Sulekar, Y. Lin, N. H. Perry and D. P. Shoemaker, *J. Am. Ceram.*
24 *Soc.*, 2019, **102**, 7210–7216.
- 25 45 R. D. Shannon, *Acta Crystallogr. Sect. A*, 1976, **32**, 751–767.
- 26 46 S. Stramare, V. Thangadurai and W. Weppner, *Chem. Mater.*, 2003, **15**, 3974–3990.
- 27 47 B. Fraygola, U. Salazar, A. Biancoli, D. Damjanovic and N. Setter, in *2013 Joint IEEE International*
28 *Symposium on Applications of Ferroelectric and Workshop on Piezoresponse Force Microscopy*
29 *(ISAF/PFM)*, IEEE, 2013, vol. 4, pp. 89–92.
- 30 48 M.-J. Pan, R. J. Rayne and B. A. Bender, *J. Electroceramics*, 2005, **14**, 139–148.
- 31 49 C. Slouka, T. Kainz, E. Navickas, G. Walch, H. Hutter, K. Reichmann and J. Fleig, *Materials*
32 *(Basel)*, 2016, **9**, 945.
- 33 50 A. Jain, S. P. Ong, G. Hautier, W. Chen, W. D. Richards, S. Dacek, S. Cholia, D. Gunter, D. Skinner,
34 G. Ceder and K. A. Persson, *APL Mater.*, 2013, **1**, 011002.
- 35 51 S. Chen, J.-H. Yang, X. G. Gong, A. Walsh and S.-H. Wei, *Phys. Rev. B*, 2010, **81**, 245204.
- 36 52 M. Geng and H. Jónsson, *Phys. Chem. Chem. Phys.*, 2019, **21**, 1009–1013.

- 1 53 P. Gorai, H. Long, E. Jones, S. Santhanagopalan and V. Stevanović, *J. Mater. Chem. A*, 2020, **8**,
2 3851–3858.
- 3 54 S. Xiong, Z. Liu, H. Rong, H. Wang, M. McDaniel and H. Chen, *Sci. Rep.*, 2018, **8**, 9146.
- 4 55 Z. Deng, J. Gu, Y. Li, S. Li, J. Peng, X. Li, J. Luo, Y. Huang, C. Fang, Q. Li, J. Han, Y. Huang and
5 Y. Zhao, *Electrochim. Acta*, 2019, **298**, 121–126.
- 6 56 R. Ubic, K. Tolman, K. Chan, N. Lundy, S. Letourneau and W. Kriven, in *Processing and Properties
7 of Advanced Ceramics and Composites V*, 2013, pp. 331–336.
- 8 57 D. Marrocchelli, N. H. Perry and S. R. Bishop, *Phys. Chem. Chem. Phys.*, 2015, **17**, 10028–10039.
- 9 58 R. Ubic, K. Tolman, K. Talley, B. Joshi, J. Schmidt, E. Faulkner, J. Owens, M. Papac, A. Garland,
10 C. Rumrill, K. Chan, N. Lundy and H. Kungl, *J. Alloys Compd.*, 2015, **644**, 982–995.
- 11 59 S. R. Bishop, D. Marrocchelli, C. Chatzichristodoulou, N. H. Perry, M. B. Mogensen, H. L. Tuller
12 and E. D. Wachsman, *Annu. Rev. Mater. Res.*, 2014, **44**, 205–239.
- 13 60 S. A. Yoon, N. R. Oh, A. R. Yoo, H. G. Lee and H. C. Lee, *J. Korean Ceram. Soc.*, 2017, **54**, 278–
14 284.
- 15 61 S.-L. Zhang, T. Liu, C.-J. Li, S.-W. Yao, C.-X. Li, G.-J. Yang and M. Liu, *J. Mater. Chem. A*, 2015,
16 **3**, 7535–7553.
- 17 62 T. Chen, G. F. Harrington, J. Matsuda, K. Sasaki, D. Pham, E. L. Corral and N. H. Perry, *J.
18 Electrochem. Soc.*, 2019, **166**, F569–F580.
- 19 63 K. H. Ryu and S. M. Haile, *Solid State Ionics*, 1999, **125**, 355–367.
- 20 64 P. Babilo, T. Uda and S. M. Haile, *J. Mater. Res.*, 2007, **22**, 1322–1330.
- 21 65 L. Sebastian, R. S. Jayashree and J. Gopalakrishnan, *J. Mater. Chem.*, 2003, **13**, 1400–1405.
- 22 66 T. Wei, L. A. Zhang, Y. Chen, P. Yang and M. Liu, *Chem. Mater.*, 2017, **29**, 1490–1495.
- 23 67 A. Boulant, P. Maury, J. Emery, J.-Y. Buzare and O. Bohnke, *Chem. Mater.*, 2009, **21**, 2209–2217.
- 24 68 Y. Wang and W. Lai, *J. Power Sources*, 2015, **275**, 612–620.
- 25 69 C. Zhang, H. Zhao and S. Zhai, *Int. J. Hydrogen Energy*, 2011, **36**, 3649–3657.
- 26 70 A. Kruth, *Solid State Ionics*, 2003, **162–163**, 83–91.
- 27 71 N. Torino, P. F. Henry, C. S. Knee, S. K. Callear, R. I. Smith, S. M. H. Rahman and S. G. Eriksson,
28 *Solid State Ionics*, 2018, **324**, 233–240.
- 29 72 N. A. Tarasova, A. O. Galisheva and I. E. Animitsa, *Russ. J. Electrochem.*, 2019, **55**, 756–761.
- 30 73 K. D. Kreuer, *Annu. Rev. Mater. Res.*, 2003, **33**, 333–359.
- 31 74 N. Bonanos, *Solid State Ionics*, 2001, **145**, 265–274.
- 32 75 Y. Yamazaki, R. Hernandez-Sanchez and S. M. Haile, *Chem. Mater.*, 2009, **21**, 2755–2762.
- 33 76 D. Han, N. Hatada and T. Uda, *J. Electrochem. Soc.*, 2016, **163**, F470–F476.
- 34 77 T. Krauskopf, S. P. Culver and W. G. Zeier, *Chem. Mater.*, 2018, **30**, 1791–1798.
- 35 78 X. He, Q. Bai, Y. Liu, A. M. Nolan, C. Ling and Y. Mo, *Adv. Energy Mater.*, 2019, **9**, 1902078.

- 1 79 J. C. Bachman, S. Muy, A. Grimaud, H.-H. Chang, N. Pour, S. F. Lux, O. Paschos, F. Maglia, S.
2 Lupart, P. Lamp, L. Giordano and Y. Shao-Horn, *Chem. Rev.*, 2016, **116**, 140–162.
- 3 80 A. Martínez-Juárez, C. Pecharrromán, J. E. Iglesias and J. M. Rojo, *J. Phys. Chem. B*, 1998, **102**,
4 372–375.
- 5 81 F. Chen, L. Xu, J. Li, Y. Yang and Q. Shen, *Ionics (Kiel)*, 2020, **26**, 3193–3198.
- 6 82 Y. Wang, W. D. Richards, S. P. Ong, L. J. Miara, J. C. Kim, Y. Mo and G. Ceder, *Nat. Mater.*, 2015,
7 **14**, 1026–1031.
- 8 83 L. J. Miara, S. P. Ong, Y. Mo, W. D. Richards, Y. Park, J.-M. Lee, H. S. Lee and G. Ceder, *Chem.*
9 *Mater.*, 2013, **25**, 3048–3055.
- 10 84 S. P. Ong, Y. Mo, W. D. Richards, L. Miara, H. S. Lee and G. Ceder, *Energy Environ. Sci.*, 2013,
11 **6**, 148–156.
- 12 85 S. Lunghammer, Q. Ma, D. Rettenwander, I. Hanzu, F. Tietz and H. M. R. Wilkening, *Chem. Phys.*
13 *Lett.*, 2018, **701**, 147–150.
- 14